Gomez-Villalba, L. S., Feijoo, J., Rabanal, M. E., & Fort, R. (2021). In-situ electrochemical synthesis of inorganic compounds for materials conservation: Assessment of their effects on the porous structure. *In Ceramics International, 47*(21), 30406–30424

DOI:10.1016/j.ceramint.2021.07.221

Ceramics International

In-situ electrochemical synthesis of inorganic compounds for materials conservation: assessment of their effects on the porous structure

--Manuscript Draft--

Manuscript Number:	CERI-D-21-05024R1
Article Type:	Full length article
Keywords:	in-situelectrochemical synthesis; pore-structure modification; Aragonite -calcite; Hydromagnesite-magnesite; Hydroxyapatite; whwellite
Corresponding Author:	Luz Stella Gomez Villalba, Ph.D. Instituto de Geociencias (CSIC,UCM) Madrid, SPAIN
First Author:	Luz Stella Gomez Villalba, Ph.D.
Order of Authors:	Luz Stella Gomez Villalba, Ph.D.
	Jorge Feijoo, Ph.D.
	Maria Eugenia Rabanal, Ph.D.
	Rafael Fort, Ph.D.
Abstract:	This study refers to the application of in-situ electrochemical synthesis as an alternative method to improve the properties of porous materials against harmful external agents that deteriorate them. It is oriented to an understanding of the effects of crystallisation on the pore structure of different compounds commonly used in the restoration and conservation of porous materials (historic ceramics, building walls, sculptures, or biomedical applications). It analyses the microstructural, chemical details, and stability of the neo-formed phases that modify the pore network. The electrochemical synthesis was carried out at ambient temperature (20°C), over high porous sandstone for crystallising Ca carbonate, Mg carbonate, Ca phosphate, and Ca oxalate compounds. Based on the neo-formed minerals, a comparison was made depending on their specific properties defining how they affected the pore structure. The characterisation included polarised light optical microscopy, environmental and field emission scanning electron microscopy, digital image analysis, cathodoluminescence(CL-ESEM),energy-dispersive X-ray spectroscopy, and X-ray microdiffraction. Aragonite, hydromagnesite, hydroxyapatite, and whewellite were identified as the majority phases depending on the treatment. Phase transformation, dehydration, and dissolution-re-precipitation processes suggested different degrees of stability, including aragonite/calcite ($CaCO_3$ treatment) and hydromagnesite/magnesite ($MgCO_3$ treatment) transformations and simultaneous crystallisation of brushite/hydroxyapatite ($(Ca_3(PO_4)_2$ treatment). Electrocrystallisation induced changes in inter-granular porosity, the development of secondary porosity inherent to the minerals, and differences in pore cementation depending on its mineralogy. Among the treatments, Mg carbonate reduced porosity most effectively, followed in descending order by calcium carbonate and calcium phosphate, being the calcium oxalate the less effective.

In-situ electrochemical synthesis of inorganic compounds for materials conservation: assessment of their effects on the porous structure

Luz S. Gomez-Villalba*

PhD. Institute of Geosciences IGEO (CSIC-UCM), c/Doctor Severo Ochoa, 7, 28040, Madrid, Spain (Phone number: +34 913 947 883). luzgomez@geo.ucm.es

gomeluz@gmail.com

ORCID 0000-0002-8755-8191

Jorge Feijoo

Ph.D. Defense University Centre, Spanish Naval Academy s/n 36920 Marin, Spain. jfeijoo@cud.uvigo.es ORCID 0000-0003-3820-5127

Maria Eugenia Rabanal

PhD. Carlos III University of Madrid. Materials Science Department and IAAB Avenida Universidad 30, Leganes, Madrid, Spain. eugenia@ing.uc3m.es, ORCID: 0000-0002-5090-6498

Rafael Fort

PhD. Institute of Geosciences IGEO (CSIC-UCM), c/Doctor Severo Ochoa, 7, 28040, Madrid, Spain. rafael.fort@csic.es ,ORCID 0000-0001-9967-2824

* *Corresponding author*

ABSTRACT

This study refers to the application of in-situ electrochemical synthesis as an alternative method to improve the properties of porous materials against harmful external agents that deteriorate them. It is oriented to an understanding of the effects of crystallisation on the pore structure of different compounds commonly used in the restoration and conservation of porous materials (historical ceramics, building walls, sculptures, or biomedical applications). It analyses the microstructural, chemical details, and stability of the neo-formed phases that modify the pore network. The electrochemical synthesis was carried out at ambient temperature (20° C), over high porous sandstone for crystallising Ca carbonate, Mg carbonate, Ca phosphate, and Ca oxalate compounds. Based on the neo-formed minerals, a comparison was made depending on their specific properties defining how they affected the pore structure. The characterisation included polarised light optical microscopy, environmental and field-emission scanning electron microscopy, digital image analysis, cathodoluminescence (CL-ESEM),energy-dispersive X-ray spectroscopy, and X-ray microdiffraction. Aragonite, hydromagnesite, hydroxyapatite, and whewellite were identified as the majority phases depending on the treatment. Phase transformation, dehydration, and dissolution-re-precipitation processes suggested different degrees of stability, including aragonite/calcite ($CaCO_3$ treatment) and hydromagnesite/magnesite ($MgCO_3$ treatment) transformations and simultaneous crystallisation of brushite/hydroxyapatite (($Ca_3(PO_4)_2$ treatment). Electrocrystallisation induced changes in inter-granular porosity, the development of secondary porosity inherent to the minerals, and differences in pore cementation depending on its mineralogy. Among the treatments, Mg carbonate reduced porosity most effectively, followed in descending order by calcium carbonate and calcium phosphate, being the calcium oxalate the less effective.

Keywords: in-situ electrochemical synthesis; porous materials, pore-structure modification; aragonite; calcite; hydromagnesite; hydroxyapatite; whewellite

1 Introduction

One of the main points of interest in studies of restoration and protection of materials is to improve their durability by modifying their porous structure. The wide field of applications covers different types of materials such as architectural structures, sculptures, palaeontological samples, or historical ceramics [1 – 11]. Also, porosity control plays a key role in the biomedical sector for dental ceramic materials [12], regenerative medicine [13], and photocatalytic applications [14].

In materials subjected to external agents, the weathering chemical processes inherent to the environment in which they are exposed [15] as well as aggressive anthropogenic agents may modify the structure of the material, leading to loss of cohesion. Water is one of the main deteriorating agents. An increase in its content may reduce the strength and rigidity of the material [16 – 19]. Modifications of pore structure produce this deterioration process leading to material fracturing due to different agents including expansion/contraction, hot/cold, freeze/thaw cycles phenomena [15,20,21] pollutants [15,22 – 27] or biological activity [28,29]. Within the archaeological ceramic pieces, the problem becomes greater since the conditions in which they have been exposed during the burial time make them quite fragile materials [30]. Its handling is delicate, and the restoration process requires special conditions and suitable effective treatments.

Until now, restoration and conservation efforts have focused on applying treatments with specific functions capable of improving the consolidation of the material or surface coatings that act against aggressive agents [31,32]. In this type of treatment, one of the main aspects to be evaluated is to improve both the hydric and mechanical behaviour. Currently, research is focused on developing new replacement materials or surface treatments capable of reducing accessible porosity to hinder and minimise the entry of water and soluble salts [33 – 35]. Within the protective treatments, there are series of inorganic mineral compounds whose application is suitable, being possible the modification of the pore structure [36]. Calcium carbonates [9] and phosphates [37 – 42] are the treatments most routinely used to consolidate building materials and works of art. Magnesium

carbonate is applied as consolidant and fire retardant [43], and calcium oxalate as patina protective in calcareous materials [44 – 46]. Although many treatments have been effective [47 – 52], they have not always achieved the expected results, being some of them of short duration or aesthetic changes inductors [53 – 57]. The application of nanomaterials has proven to be effective as long as the most compatible products are applied [58 – 63].

Electrochemistry has made significant progress in different applications, highlighting the synthesis of inorganic compounds with specific properties [64 – 68]. In the field of materials conservation, different techniques are currently being developed [69 – 71], many of which have to be carried out with specific devices [72]. Amongst the different variants, in situ electrochemical synthesis allows the modification of materials to improve their specific properties [73 – 76].

In the consolidation of deteriorated materials, promising results have been obtained from inorganic compounds of low solubility to reduce the accessible porosity [77,78]. However, evaluating the effect of the different treatments on porosity is still challenging.

This research aims to contribute to an understanding of the effects of crystallisation by applying the in-situ electrochemical synthesis technique to different minerals commonly used in restoration treatments. Furthermore, it is intended to control the growth and modification of the pore structure, in a high purity sandstone. This synthesis technique is presented as an alternative method to improve the properties of porous materials against harmful external agents that may induce their deterioration.

2. Methodology

2.1 Synthesis process

In situ electrochemical synthesis was carried out to crystallise inorganic compounds of calcium carbonate, magnesium carbonate, calcium phosphate, and magnesium oxalate. This process consisted of establishing an electrical field to force ion mobilisation between opposite poles across percolating pores in a quartz arenite sandstone with high content of porous [77]. The high contrast

provided by the texture of this material facilitates the identification of the different compounds synthesised.

The stone was quarried from an area just north of Copenhagen. This type of material was used to build Kronborg Castle at Elsinore, Denmark.

Elecrocrystallisation was performed on a sandstone specimen (10×10×6 cm) coupled with a series of compartments for both the anode and the cathode, using titanium working electrodes. Each of the compartments consisted of three cells separated by cellulose membranes connected to a direct current (DC) source. Both at the anode and the cathode, two of the cells were filled with specific solutions according to each compound, while the intermediate cell was filled with a poultice. This poultice was kept humidified during the process with a solution of kaolin and ultrapure water (1.5:1.0 weight ratio), to facilitate the transport of electricity, and buffer the extreme pH values caused by electrolysis in the electrodes. Details of the synthesis device are described in [79].

Elecrocrystallisation was made in two steps, an initial one with a current direction from anode to cathode and a second in the opposite direction. A constant current of 12V was applied with an intensity close to 10mA. The precursors used for the crystallisation of the different compounds and the different phases that can result from the electrochemical reaction are summarised in Table 1.

Table 1 Experimental conditions at 25°C and possible crystallised minerals

Treatment	**Anode**	**Cathode**	**Stoichiometric Formula**	**Compound**	**Mineral**
Ca carbonate	$(NH_4)_2CO_3$ 0.5 M pH 8.9	$Ca(CH_3CO_2)_2$ 0.5 M pH 7.3	$CaCO_3\ nH_2O$	$CaCO_3$ $CaCO_3 \cdot H_2O$ $CaCO_3 \cdot 6H_2O$	Calcite, Aragonite, Vaterite Monohydrocalcite Ikaite
Mg Carbonate	$(NH_4)_2CO_3$ 0.5M pH 8.9	$Mg(CH_3CO_2)_2$ 0.5M pH 7.3	$Mg_y(CO_3)_z(OH)_x$ nH_2O	$Mg_5(CO_3)_4(OH)_2 \cdot 4H_2O$ $MgCO_3$ $Mg_5(CO_3)_4(OH)_2 \cdot 5H_2O$	Hydromagnesite Magnesite Dypingite
Ca Phosphate	$(NH_4)_3PO_4$ 0.5M Na_3PO_4 0.2 M pH 7.5	$Ca(CH_3CO_2)_2$ 0.5M, pH 7.3	$Ca_{(3+1/2x)}(PO_4)_2$ $(OH)_x\ nH_2O$	$Ca_5(PO_4)_3(OH)$ $Ca(PO_3OH)\ 2H_2O$ $Ca(H_2PO_4)_2 \cdot H_2O$ $Ca(H_2PO_4)_2$ $CaHPO_4\ H_2O$ $CaHPO_4$ $Ca_8H_2(PO_4)_6 \cdot 5H_2O$ $Ca_3(PO_4)_2$ $Ca_xH_y(PO_4)_2 \cdot nH_2O$ $Ca_4(PO_4)_2O$	Hydroxylapatite DCPD Brushite Monocalcium phosphate Monohydrate Monocalcium phosphate anhydrous Dicalcium phosphate monohydrate Dicalcium phosphate anhydrous Octa-calcium phosphate α, α´β tricalcium phosphate Amorphous calcium phosphate Tetra-calcium phosphate
Ca Oxalate	$(NH_4)_2C_2O_4$ 0.2M + Na_3PO_4 0.2M pH 7.3	$Ca(CH_3CO_2)_2$ 0.5M pH 7.3	$CaC_2O_4.nH_2O$	$CaC_2O_4 \cdot H_2O$ $CaC_2O_4 \cdot 2H_2O$ $Ca(C_2O4)\ 3H_2O$	Whewelite Weddellite Coexite

2.2 Characterisation

The assessment of the electro crystallisation process was carried out by comparing the electrochemically treated samples with an untreated reference specimen. Characterisation included petrographic and mineralogical studies with polarised light optical microscopy (PLOM), field emission scanning electron microscopy (FESEM), environmental scanning electron microscopy (ESEM), energy-dispersive X-ray spectroscopy (EDS), X-ray microdiffraction (micro-XRD), and cathodoluminescence spectroscopy (ESEM-CL). The digital image analysis (DIA) technique was used to evaluate the modifications in the pore structure using FESEM images taken with secondary electron (SE) and backscattered electron (BSE) detectors.

The petrographic analysis by PLOM was performed from thin sections previously dyed with methylene blue to highlight porosity and polished down to 30µm, using an Olympus BX 35 polarised light petrographic microscope fitted with Stream Essential software for image analysis. High resolution SEM studies were conducted on a FEG-SEM Teneo LoVac (FEI-Thermo Fisher Scientific operating at 10kV, 0.2-0.8nA, equipped with an EDS (EDAX) probe. The environmental scanning electron microscopy was performed in a FEI Inspect ESEM equipped with an EDS (oxford instruments analytical INCA) probe operating in low vacuum mode.

The chemical analysis was carried out by energy dispersive X ray spectroscopy (EDS). It was used to calculate the Ca/O/C (calcium carbonate treatment), Mg/O/C (magnesium carbonate treatment), Ca/O/P (calcium phosphate treatment), and Ca/O/C (calcium oxalate treatment) ratios and comparing the values found to the data published by the Mineralogical Society of America [80] and the online mineralogy database[81]. The microscopic analysis was carried out in different orientations to guarantee better control of the textural and mineralogical properties before and after treatments.

In situ identification of minority phases in specific regions of the sample was fulfilled using the X-ray microdiffraction technique, which allows more information than conventional X-ray diffraction (total scan) [82,83]. X-ray microdiffraction analyses were recorded on a Philips X'Pert X-ray

diffractometer operating in a continuous mode, over a 2θ range of 5° to 60° with a 0.016° step size and a 149.86s count time per step. Micro XRD data were analysed with the American Mineralogist Crystal Structure Database (AMCSD) [84] and the X´pert High Score Plus software endorsed by the ICDD (International Centre for Diffraction Data).

Spectral cathodoluminescence-SEM (CL-SEM) technique was used to identify the different minerals including the eventual polymorphism, and to monitor phase transformation processes [85]. It was run on a Gatan MONO CL3 cathodoluminescence detector coupled to the FEI Inspect ESEM microscope. CL provided information about the chemical composition from intrinsic and extrinsic transitions which alter the local optical properties of the material [86]. These signals helped to identify internal defects or trace elements in the neoformed minerals.

3. Results and discussion

3.1 Mineralogical and textural analysis

3.1.1 Untreated sandstone

The textural and mineralogical properties of the untreated sandstone are depicted in Fig. 1. The overview in the PLOM image (Fig. 1a) revealed sub-angular to sub-round quartz grains. Inter-granular pores (blue), some partially filled with kaolinite-like clay minerals (K) were identified. SEM images (Fig. 1b and 1c) showed the quartz-arenite texture and respective inter-granular pores, partially filled with kaolinite (K). The processed image (Fig. 1d) highlights the inter-granular porosity (green) and the clay-like minerals (red) present. In the surface roughness intensity profile (Fig. 1e), the dark tones represent pores and the light tones quartz grains. Grain and pore size are summarised in Tables 2 and 3. In the micro XRD pattern (Fig. 1f) the highest intensity peaks correspond to low-quartz (JCPDF 86-1630, a=b=4.914Å, c=5.406Å, hexagonal symmetry). A smaller percentage of kaolinite-like phyllosilicates (JCPDF 01-080-0886; a=5.1577Å; b=8.9417Å; c=7.3967Å; triclinic symmetry) was also confirmed. The corresponding ESEM-

cathodoluminescence spectrum (Fig. 1f) at λ=380nm, 460nm, and 636nm correspond to defects as reported by other authors (Table 4).

Table 2 Particle size (μm) of electrocrystallised and original sandstone minerals

		Mineral	Dimension	Mean Particle size (μm)	Standard Deviation (μm)
Original minerals in sandstone		Quartz	Length	101.0	32.0
			Width	66.1	27.8
		Kaolinite	Length	4.1	1.2
			Width	2.8	0.9
Electrocrystallised minerals	Ca carbonate	Aragonite	Length	9.9	15.6
			Width	1.07	1.1
		Calcite	Length	3.5	0.5
			Width	2.4	0.38
	Mg carbonate	Hydromagnesite	Length	20.7	20.0
			Width	1.9	1.5
		Magnesite	Length	4.1	0.9
			Width	2.8	0.9
	Ca Phosphate	Hydroxyapatite	Length	21.2	11.6
			Width	0.4	0.1
	Ca Oxalate	Whewellite	Length	2.1	1.4

3.1.2 Calcium carbonate electrocrystallisation

The results of calcium carbonate electrocrystallisation are reproduced in Figs. 2 and 3. The overview in the PLOM image (Fig. 2a) revealed the presence of fibrous calcium carbonate crystals (cc) partially occupying the pores (blue) between quartz grains (Qz). SEM images (Figs. 2b and 2c) show different anhydrous calcium carbonate polymorphs, including aragonite (Ar), calcite (calc), and amorphous calcium carbonate (ACC). The aragonite plates prevailed along with small calcite crystals and occasionally, surfaces occupied by amorphous calcium carbonate denoting different degrees of crystallinity in the system, as well as crystallisation of the most stable of calcium carbonates, calcite. Aragonite crystallisation (Figs. 2c and 2d) showed radial growth on pore surfaces. The presence of aragonite, calcite, and kaolinite was confirmed by X-ray microdiffraction (Fig. 4a). Further to the roughness intensity profile (Fig. 2e), inter-granular space and intercrystalline porosity are identified. Such secondary porosity consists in the space between aragonite fibres. The processed image (Fig. 2d) shows that aragonite occupied 78% of the pore surface. Particle size and pore dimension measurements are listed in Tables 2 and 3.

Fig. 3 contains more detailed porosity images, with higher magnification of both inter-granular and secondary intercrystalline porosity. The SEM image (Fig. 3a) and as processed (Fig. 3b) showed that the pore surfaces were occupied by aragonite. Calcite, with much smaller crystals, occupied the aragonite intercrystalline spaces, obstructing the pores and preventing aragonite crystals from occupying the entire pore surface. The secondary honeycombed intercrystalline porosity visible in some areas was generated by variously oriented aragonite fibres (Fig. 3c). The enlarged image (Fig. 3d) reveals calcium carbonate (Cc) intergrowth in areas characterised by hexagonal kaolinite (K) plates present in the original stone, along with local secondary porosity induced by neo-mineralisation.

The microdiffraction pattern confirmed the prevalence of aragonite (JCPDF 00-041-1475, a=4.96Å, b= 7.96Å, c=5.7439Å, space group: Pmcn, orthorhombic symmetry) and lower intensity signals indicative of calcite (JCPDF 00-005-0586, a=4.98 Å, b= 4.98 Å, c=17.06 Å, Space group: R-3c, rhombohedral symmetry), together with kaolinite (JCPDF 00-005-0143 a=5.14Å, b=8.93Å, c=7.37Å, anorthic symmetry) (Fig. 4a). The corresponding cathodoluminescence spectrum in the λ=300nm to 380nm range suggested the presence of defects in aragonite and calcite crystals (Fig. 4b), as reported in other materials (Table 4). EDS chemical analysis (Fig. 4c) depicted in the form of the Ca/O/C ternary diagram showed that most of the neo-formed crystals were located in areas with a prevalence of anhydrous calcite polymorphs (calcite, aragonite, and vaterite), although monohydrocalcite-like (Group 1) hydrated phases were also locally present. A few analyses identified regions with excess calcium (Group 2), possibly in areas with more structural defects that tend to have a higher cation concentration.

3.1.3 Magnesium carbonate electrocrystallisation

The magnesium carbonate-treated sandstone is depicted in Fig. 5. In addition to quartz (Qz) and kaolinite (K), the PLOM image revealed fan-shaped crystals in the pore space (blue), identified with X-ray microdiffraction as hydromagnesite (HM) (Fig. 6), the most prominent crystallised precipitate. The SEM image (Fig. 5b) confirmed the presence of fibrous crystals occupying the

pores between quartz (Qz) grains. In addition to HM, hexagonal magnesite crystals (were attached to the fibre surfaces on the outer edges of the pores. Hydromagnesite dehydration induced local transformation to magnesite, the most stable of the magnesium carbonate polymorphs. The HM plates proved to be flexible, growing along the longer pore dimension (Fig. 5c) and occupying up to 68% of the surface (Fig. 5d), processed image. The roughness intensity profile, drawn for a cross-section perpendicular to the direction of the fibres (Fig. 5c) revealed the presence of inter-granular pores and inter-crystalline pores. Crystallisation details are visible in the enlarged images in Fig. 6. Fig. 6a shows the hydromagnesite fibres in quartz intergranular spaces, along with the local dissolution and reprecipitation that reduced the pore size (as observed in Fig. 6b). Particle size and pore dimension measurements are summarised in Tables 2 and 3.

The X-ray microdiffraction pattern for a crystallised area confirmed the presence of hydromagnesite (JCPDF 00-025-0513, a=10.1Å, b= 8.9Å, c=8.3Å space group: P2_1/c, monoclinic symmetry) and magnesite (JCPDF 01-071-1534, a=4.6Å, b=4.6 Å, c=15.02Å, Space group: R-3c, rhombohedral symmetry) in sandstone. The corresponding cathodoluminescence spectrum in the λ= 300nm to 500nm range (Fig. 7b) suggested the presence of defects in the hydromagnesite and magnesite crystals as reported in other materials (Table 4). Differences in solubility of hydromagnesite concerning magnesite (hydromagnesite < magnesite) must be borne in mind when analysing dissolution of the former in its transformation to the latter [87]. In the dissolution-reprecipitation reaction, magnesite only grows when the system reaches equilibrium. The possible existence of mass transfer and the concomitant concentration gradient would favour the appearance of defects in the resulting precipitates [87].

EDS chemical analysis (Fig.7c) showed the experimental data to be located in the area where hydromagnesite and magnesite crystallised, as observed on the Mg/O/C ternary diagram.

3.1.4 Calcium phosphate electrocrystallisation

The PLOM image (Fig. 8a) revealed the presence of minerals from the apatite group, identified as brown grains, which appear to fill the pores. It is presented as microcrystalline calcium phosphate

and fibrous calcium phosphate clusters. The fibrous crystals stretching parallel to the longer pore dimension in the enlarged images (Fig.s 8b and 8c) grew epitaxially around the edge of the pore surface delimited by the quartz grains. They tended to fill the pore in line with the longer dimension. Hydroxyapatite was also observed to grow in the spaces previously filled by hexagonal kaolinite foils (Fig. 8b). According to the processed image data, hydroxyapatite occupied up to 89% of the pore surface (Fig. 8d). The X-ray microdiffraction findings confirmed the presence of hydroxyapatite as well as of other apatite group polymorphs with dicalcium phosphate dihydrate (DCPD, also known as brushite) (Fig. 10a). Particle size and pore dimension measurements are listed in Tables 2 and 3.

Hydroxyapatite was observed to occupy the pore surface although not in all the pores (see SEM image in Fig. 9a) and respective processed image in Fig. 9b),. The presence of both inter-granular and intercrystalline porosity was confirmed by the roughness intensity profile (Fig. 9c) in a cross-section of the pore parallel to its long dimension. Short fibrous crystals with a petal-like habit were also observed and identified as dicalcium phosphate dihydrate (DCPD). The fibres were assembled in ways that favoured the appearance of secondary porosity (Fig. 9d).

The X-ray microdiffraction pattern (Fig. 10a) confirmed the presence of hydroxyapatite (JCPDF 01-073-0293, a=9.4Å, b=9.4Å, c=6.8, Space group: P63/m, hexagonal symmetry) and brushite, DCPD (JCPDF 01-072-0713, a=5.812Å, b=15.180Å, c=5.180Å, Space group: Ia, monoclinic symmetry) and quartz. The corresponding ESEM cathodoluminescence spectrum (Fig. 10b) denoted changes in the λ= 300nm to 500nm range, which corresponds to defects in the hydroxyapatite crystals and other apatite polymorphs as was reported in other materials (Table 4). EDS chemical analysis (Fig. 10c) delivered values that lay in the area where hydroxyapatite ($Ca_5(PO_4)_3(OH)$ [80], Group 1) and other apatite group polymorphs crystallised, as observed on the P/O/C ternary diagram. Hydroxylapatite is cited in some cases as $Ca_{10}(PO_4)_6(OH)_2$ to indicate that the crystal unit cell is a dual structure [88]. Although hydroxyapatite was the predominant phase, evidence was observed of different degrees of hydration due to local differences in water content, as shown by the XRD

identification of DCPD. Some analyses also revealed areas with an excess of P ions (Group 2), possibly the result of higher proportions of structural defects that induced cationic disorder.

Table 3 Pore size before and after electrocrystallisation

		Dimension	**Mean Pore size (µm)**	**Standard Deviation (µm)**
Pore size in sandstone before electrocrystallisation		Length	93	38
		Width	30	20
Pore size after electrocrystallisation	Ca carbonate	Length	59	36
		Width	31	28
	Mg carbonate	Length	67	36
		Width	34	32
	Ca Phosphate	Length	68	35
		Width	36	18
	Ca Oxalate	Length	78	44
		Width	36	25

3.1.5. Calcium oxalate electrocrystallisation

The treatment with calcium oxalates induced partial mineralisation in some of the sandstone pores (Fig. 11a, PLOM image). The SEM image (Fig. 11b) depicts the local positioning of the calcium oxalates (C-Ox) crystals in a pore. C-Ox precipitated on the pore walls, occupying 9% of the surface (Fig. 11c) and giving rise to new porosity. Whewellite only fills in small pores. The small size of the minerals blocks the crystallisation advance in such a way that the pores appear partially filled (pore-clogging). These crystals were observed to dissolve, generating further porosity. The processed image (Fig. 11d) showed the position and orientation of the C-Ox crystals along the quartz grain edges, as well as the presence of intercrystalline porosity. Details of pore filling are shown in the roughness intensity profile (Fig. 11e) taken along the cross-section defined in Fig. 11c. Particle size and pore dimension measurements are listed in Tables 2 and 3. The enlarged images (Fig. 12a and b) depict whewellite dissolution after precipitation in the sandstone pores. Details such as locally present hexagonal kaolinite (K) plates can also be discerned in Fig. 12a.

The X-ray microdiffraction pattern (Fig. 13a) confirmed whewellite (Wh) to be the prevalent phase, as well as the presence of quartz (Qz) and kaolinite (K). The ESEM cathodoluminescence spectrum denoted changes in the signals for the sample treated with calcium oxalate (Fig. 13b).The bands in the λ= 300nm to 500nm range suggested the presence of defects in the crystallised minerals as reported in other materials (Table 4). EDS chemical analysis delivered values that lay in the area where whewellite ($Ca(C_2O_4)\cdot(H_2O)$) crystallised, although depending on local water content, hydrated calcium oxalates ($CaC_2O_4.nH_2O$) such as weddellite and caoxite (Table 1), below the XRD detection limit, may also crystallise, as observed on the Ca/O/C ternary diagram.

Table 4 Experimental cathodoluminescence- ESEM emission and references

Treatment	Experimental λ (nm)	Experimental λ (eV)	Reference λ (nm)	Assignation	Mineral	Reference
Untreated sandstone	380	3.26	380	Defect	Quartz	[89,90]
	460	2.69	460	Intrinsic	Quartz	[89]
	636.5	1.93	642	Non-Bridging Oxygen Hole ~NBOHC	Quartz	[89,91]
Ca carbonate	366	3.38	366	Intrinsic	Calcite	[92]
	358	3.46	358	Intrinsic defects at grain boundaries and cracks and non-bridging oxygen hole centres	Aragonite	[93]
	360	3.44	358	Crystal defects	Aragonite	[94]
	375	3.30	375	Defect centers	Calcite	[95]
	378	3.28	378	Oxigen deficient centers-Non-Bridging Oxygen Hole ~NBOHC	Calcite	[92]
Mg carbonate	424.5	2.91	425	Intrinsic	Magnesite	[96]
	441	2.81	440	unspecified	Magnesite	[97,98]
	452, 465	2.74, 2.66	458, 465	unspecified	Hydromagnesite	[99]
Ca Phosphate	390	3.18	390	O^{-2} intrinsic defects	Hydroxyapatite	[100]
	400	3.1	400	Lattice defects	Anhydrous apatite $(Ca_5(PO_4)_3$	[101,102]
	420	2.95	420	intrinsic	Hydroxyapatite	[103]
	433	2.85	431	structural defects	Hydroxyapatite	[104]
Ca Oxalate	414	2.99	410	Intrinsic	Whewellite	[105]
	434	2.81	434	NBOHC oxygen deficiency centres Vacancies	Whewellite	[106]
	471	2.63	471	Defects	Whewellite	[106]

3.2 Comparison of treatments and their effects on pore structure

As a result of electrocrystallisation with calcium carbonate (Fig. 14b), the pores filled up with calcium carbonate polymorphs, primarily aragonite (Ar). Calcium carbonate did not fill the pores entirely, although it did lower porosity from 19.5% in the untreated sandstone to 12.1%. Porosity was defined to include both inter-granular and a secondary, intercrystalline type porosity induced by neo-mineralisation. After electrocystallisation with magnesium carbonate (Fig. 14c), hydromagnesite (HM) was the predominant phase, reducing (inter-granular plus intercrystalline) porosity to 10.5 %

Nonetheless, the surface around the edges of the quartz grains (green) was observed to be incompletely filled. With calcium phosphate treatment (Fig. 14d), hydroxyapatite (HAP) was observed to cover pore walls while leaving a substantial portion of the pores unfilled, with total porosity amounting to 13.8% after treatment. Fig. 14e) shows that as calcium oxalate (whewellite, C-Ox) filled only some of the pores, the total reduction in porosity was small, to just 18.4%.

The statistical findings revealed a series of differences in terms of the effect of treatment mineralisation, as summarised in Fig. 15. In addition to inter-granular porosity (Fig. 14 and Fig. 15a), differences in intercrystalline porosity increased total porosity. Magnesium carbonate electrocrystallisation reduced inter-granular and intercrystalline porosity more than any other treatments, followed in descending order by calcium carbonate, calcium phosphate, and calcium oxalate (Fig. 15a). The percentage of pores filled (Fig. 15b) was also highest with magnesium carbonate, at 55%, whereas calcium oxalate lowered the number by a mere 7.8%.

Pore surface fill differed with the treatment applied (Fig. 15c). When electrocrystallisation was conducted with calcium phosphate 89% of the pore surface was mineralised. With calcium carbonate 78% of the surface was occupied, and with magnesium carbonate, 68%, whilst with calcium oxalate, only 9% of the surface was affected.

The treatments studied exhibited similarities and differences in terms of the modification of mean inter-granular pore size in the untreated sandstone (Fig. 15d). Calcium carbonate lowered size most significantly.

A comparison of the size of the neo-formed crystals based on the SEM image findings (Fig. 15f and 15g) revealed the mean lengths of the fibrous hydroxyapatite and hydromagnesite to be very similar, although particle size varied in the latter over a wider range, from a maximum 40μm to a minimum of 8μm. The mean size in the aragonite crystals was around 10μm, whilst at ~6μm, it was much smaller in calcium oxalate than in any of the other phases. The hydromagnesite crystals had much wider fibres than the hydroxyapatite crystals (~2 μm compared to 0.8 ~μm). Particle size data for the crystals are summarised in Table 2.

Several factors were found to affect pore fill significantly. Crystal growth kinetics differ and depend, in addition to chemical composition, on other characteristics that must be borne in mind, including morphology, particle size, local pH, intrinsic porosity, and solubility.

The conspicuous reduction in pore size in the sandstone treated with calcium carbonate might be related to the nucleation of its various polymorphs, with aragonite and occasionally calcite forming in areas initially containing amorphous carbonate. Calcite crystals were much smaller than aragonite and in some areas co-existed with aragonite crystals, although when calcite concentration was higher, cementation caused local pore obstruction that hindered aragonite crystal growth.

Electrocrystallisation with magnesium carbonate and calcium phosphate effectively prompted substantial pore fill. As the hydroxyapatite crystals were much narrower (Fig. 15g), they could occupy smaller inter-granular spaces and adapt to different surfaces, filling 89% of the pores, compared to the 68% observed with hydromagnesite. Pore surface cover was intensified by the local presence of smaller, fibrous DCPD crystals. Although a greater pore surface was occupied with calcium phosphate, porosity (10.5%) was lower in the treatment with magnesium carbonate than with calcium phosphate (13.8%). Differences in the physical-chemical properties of the two phases affected crystallisation kinetics. As noted, being more soluble than hydroxyapatite,

hydromagnesite gave rise to dissolution and re-precipitation, both of which favour a reduction in porosity, whereas no such effect was observed in the nearly insoluble hydroxyapatite. In addition, the flexibility of the hydromagnesite fibres and the particle size distribution of its crystals contributed to greater diffusion across the pores.

In electrocrystallisation with calcium oxalate, the short, neo-formed prismatic crystals grew on but failed to fill pore surfaces. The local clogging that ensued hindered further crystallisation due to the small size of the crystals, with only 9% of the pores ultimately filled. The narrowest pore surfaces were filled and gave place to bottlenecks among the interconnected pores. In this way, fluid migration decreased, such it has been described in distinct mineral precipitation and dissolution processes [23,107].

In the untreated sandstone, kaolinite-like phyllosilicates that filled the pores were observed to co-exist with the neoformed minerals. Their arrangement in stacked hexagonal plates appeared to favour calcite (calcium carbonate treatment) and whewellite (calcium oxalate treatment) precipitation. Earlier studies showed that clay minerals might serve as templates for phase precipitation [108].

3.3 Mineral Properties

The minerals crystallising in magnesium carbonate, calcium phosphate, and calcium oxalate systems consisted in hydrated phases: hydromagnesite, hydroxyapatite and whewellite. Evidence was found, however, of local phase change, with hydromagnesite-to-magnesite dehydration, simultaneous crystallisation of hydroxyapatite- and -dicalcium phosphate dehydrate, and variations in calcium carbonate crystallinity ranging from the amorphous state to aragonite and from the latter to calcite.

Crystallisation kinetics depended in each mineral system on several intrinsic and extrinsic factors, including temperature and pH [109–112]. Local changes in fluid stoichiometry and saturation degree where deposition takes place may likewise favour the precipitation of a given mineral [113].

Dissolution-reprecipitation is associated with specific conditions such as particle size and shape [114] or declining pH values [112].

According to the solubility values reported in earlier studies for the minerals analysed, magnesite is the most and hydroxyapatite the least soluble, in the following order: magnesite> whewellite>calcite>aragonite> hydromagnesite> hydroxyapatite [115,116].

Solubility itself depends on other factors, however [117], including pH and particle size, inversely in the latter case, with solubility rising at smaller sizes [109,114,116,118,119]. It is also impacted by metastable phase crystallisation and local stoichiometric changes [120,121]. Solubility studies [122] have shown that the presence of defects in the crystalline network induces dissolution or even loss of crystallinity.

The presence of defects in the neoformed minerals attested to by the ESEM-cathodoluminescence findings (Table 4) would favour mineral reactivity, hastening phase transformation [123], or dissolution-reprecipitation [122]. The development of porosity due to relative differences in solubility, the formation of fractures, and/or the presence of grain boundaries may favour fluid access [124].

Further to earlier reports, the mass transfer may be associated with the dissolution-reprecipitation process [87]. Mass transfer can also be applied to electrocrystallisation and, may lead to local stoichiometric change and hence to defect generation.

As such mass movements from one position to another and concomitant stoichiometric change would have taken place in all the treatments analysed here, the resulting concentration gradients would be expected to give rise to defects.

Of all the phases crystallising in the various systems studied here, treatment with magnesium carbonate reduced porosity most effectively, followed in descending order by calcium carbonate, calcium phosphate, and calcium oxalate.

The dissolution-reprecipitation observed in hydromagnesite-bearing pores was a determinant in lowering porosity. Although the magnesium carbonate precipitation rate is much slower than

recorded for calcium carbonate [125], crystal size has a significant effect on pore structure. Further to the present observations, particle size and with its reduction in porosity was greater in hydromagnesite than in any of the other neoformed minerals.

In a similar vein, in electro-precipitation with calcium oxalates, whewellite particle size clogged the pores. However, its dissolution did not have a favourable effect on reducing porosity, filling only the smallest pores, as noted by previous authors. [126]. Establishing the origin of such differences would entail exploring the specific conditions that affect the presence or otherwise of certain phases in each system.

Depending on the electrochemical treatment it can be identified different factors affecting crystallisation on the pore structure as discussed below:

- *Calcium carbonate treatment*: The different polymorphs extant in the calcium carbonate system, including hydrated metastable phases and amorphous carbonate (Table 1), are indicative of variations in their stability [102,104]. In the present study, aragonite was the majority phase identified, along with local calcite crystallisation and less crystallised areas exhibiting amorphous calcium carbonate. Earlier studies showed that the presence of defects in the atomic network in aragonite favour the transformation of the mineral to calcite [127]. Metastable hydrated phases may have crystallised, however, depending on the local concentration of hydroxyl ions that lie below the detection limit of micro XRD.

- *Magnesium carbonate treatment*: Differences in the polymorphs and hydrated phases, the most stable of which is hydromagnesite [128,129], including magnesium carbonate hydroxyhydrates, have been reported in the magnesium carbonate system (Table 1) [130]. With dehydration hydromagnesite converts to the most stable anhydrous phase, magnesite ($MgCO_3$). Dehydration to magnesite has been observed to be a relatively slow process, however [128]. Furthermore, in magnesium carbonate hydrates both the H_2O and hydroxyl ion content as well as temperature play a significant role in morphology [131].

- *Calcium phosphate treatment*: Calcium phosphate crystallisation may include intermediate phases which appear before the system stabilises fully [132] (Table 1). Eleven minerals have been reported in the calcium phosphate system, depending on the Ca/P molar ratio, which may vary from 0.5 to 2.0. Their stability depends on the degree of hydration and temperature [133]. Hydroxyapatite was the major phase precipitating in this study, a finding consistent with its status as one of the most stable calcium phosphate polymorphs [134]. Depending on the hydroxyl ion or water molecule content, tri- and dicalcium phases or anhydrous calcium phosphate (β -, α and α′) may form, with crystallisation taking place at different temperatures and stability heavily dependent on ionic substitution [135]. Brushite was the phase identified here by X-ray microdiffraction, although the local presence of stoichiometric variations generating other metastable hydrated phases below the detection limit cannot be ruled out. The simultaneous presence of hydroxyapatite and brushite is quite common. Within the minerals of the apatite group, a variation in the c/a lattice parameters can give rise to different Ca phosphates, including those with hydroxyl-bearing varieties of apatite, many of them with the cryptocrystalline appearance as observed by PLOM [136].

The growth rate and specific morphological details of calcium phosphates denote their dependence on pH and other environmental conditions. Fibrous hydroxyapatite may form fairly quickly in media with a pH of around 9 or 10 [137], which is consistent with the present findings. Hydroxyapatite stability depends on the crystal plane (010 and 001). Further to recent studies, plane 010 is more stable, a finding of particular importance in biomineralisation and bone repair research [134]. In a moist environment, crystallised calcium phosphate phases may be readily modified by local variations in the Ca/P ratio [138]. However, as noted earlier, hydroxyapatite solubility is also conditioned by factors such as pH, stoichiometry, and particle size [118,119]. Brushite was identified in other studies at pH<7, with a greatest stability found at pH<5 [139]. Research conducted on different calcium phosphates in which pH varied locally has shown crystallisation to be attendant upon a decline in pH [132]. In this study, the presence of DCPD was an indication that the pH declined locally during electro-crystallisation. Confinement in the sandstone pore structure

favoured the presence of that phase, as reported by other authors [140]. The pH value also affected crystal morphology, which ranged from petal-like in acidic environments (pH=4.5-6) to prism-like in more neutral (pH~7) media [141]. The brushite observed here exhibited a petal-like habit, suggesting a local decline in pH due to inside-pore confinement.

- *Calcium oxalate treatment*: Different compounds with varying degrees of hydration have been reported in the calcium oxalate system. The most thermodynamically stable is calcium monohydrate, also denominated whewellite ($CaC_2O_4 \cdot H_2O$), followed by metastable calcium dihydrate (weddellite, $CaC_2O_4 \cdot 2H_2O$) and calcium trihydrate (Table 1). Phase transformation depends on the degree of hydration, which may impact growth rate and dissolution [142,143]. Calcium monohydrate has a monoclinic symmetry, whereas calcium dihydrate is tetragonal, giving rise to several shapes. Calcium oxalate hydrate solubility and instability rise with the amount of water of crystallisation. Water molecule loss in calcium trihydrate generates calcium mono- or di-hydrate [144]. The present findings suggest greater system stability with the precipitation of the most stable phase, whewellite.

Another criterion to be borne in mind in this regard is the difference in specific physical-chemical properties between the neoformed minerals, for that parameter has been shown to be highly dependent on both particle size distribution and precipitation rate. Higher suspension density gives rise to improvements in pore size distribution [145]. The findings showed a very narrow range of hydroxyapatite crystal size.

Similar to these findings, the prevalence of fibrous habit crystallisation in calcium carbonate, magnesium carbonate and calcium phosphate systems has been identified in other electro-chemical-based treatments [110,111]. Since crystallisation in each treatment is directly related to diverse factors [80,118,127–129], pore structures may be modified in each system to afford the material at issue the specific properties desired

4. Conclusions

As a consequence of the electrochemical synthesis, the following conclusions stand out:

1 The in-situ electrochemical synthesis led to an understanding of the mechanisms involved in the mineralisation induced by the various treatments and their effect on sandstone pore structure. The methodology used in the present work could be applied in different building and ceramics materials where the modification of the pore structure is essential to obtain the desired properties for its potential use as consolidants or protective treatments.

2 Elecrocrystallisation allowed forming stable mineral phases in each treatment. Aragonite prevailed in the Ca carbonate, hydromagnesite in the Mg carbonate, hydroxyapatite in the Ca phosphate, and whewellite in the Ca oxalate system. In-situ phase transformation impacted the degree to which the minerals filled the pore areas and consequently modified pore structure.

3 The degrees of structural stability identified in the neoformed phases displayed the presence of amorphous calcium carbonate, aragonite and calcite polymorphs in stone treated with Ca carbonate. Dehydration suggested changes in local pH conditions during electro-crystallisation, confirming hydromagnesite-to-magnesite phase transformation in stone treated with Mg carbonate or brushite and hydroxyapatite crystallisation when the stone was treated with Ca phosphate.

4 The pore system was affected both by the specific morphology and crystal size of each neoformed mineral. In the pore filling process, two different trends were observed in the treatments that resulted in fibrous crystals and the formation of short prismatic ones. In the former, fibrous crystals grown along the longest pore axis of elongated pores. This filling is associated with the electro-crystallisation of hydromagnesite, aragonite and hydroxyapatite. In the second case, short prismatic crystals of whewellite only covered the pore rim. There was also a tendency to develop intercrystalline porosity within the neoformed crystals. This kind of secondary porosity was formed between the grain boundaries of individual crystals,

unlike the intergranular porosity formed between quartz grains. Intercrystalline porosity was visible amongst prismatic aragonite crystals, hydromagnesite and hydroxyapatite fibres.

5 Porosity was reduced more effectively by fibrous than by short prismatic crystals, whilst the broadest range of particle sizes was observed for hydromagnesite fibres. Elecrocrystallisation produced changes in inter-granular porosity, and differences in pore cementation depending on its mineralogy. Among the treatments, Mg carbonate reduced porosity most effectively, followed in descending order by calcium carbonate and calcium phosphate, being the calcium oxalate the less effective. The dissolution-reprecipitation observed in the Mg carbonate system determined its greater efficacy in reducing porosity than the other treatments. At the same time, dissolution, in conjunction with the small size of the whewellite crystals, prevented the advance of mineral fluids to the larger pores producing bottlenecks and pore-clogging. These factors would explain the scant reduction in porosity delivered by the calcium oxalate treatment.

6 The crystallised phases exhibited intrinsic cathodoluminescence signals due to structural defects which may favour mineral reactivity, including dissolution and reprecipitation processes

Funding
This work was funded by the following projects: TOP-HERITAGE- (Technologies in Heritage Sciences (S2018 / NMT_4372, Community of Madrid); MULTIMAT CHALLENGE: Materiales Multifuncionales para los retos de la Sociedad (S2013/MIT-2862, Community of Madrid); Additive Manufacturing: from material to application, ADITIMAT-CM (S2018/NMT-4411, Community of Madrid); MAT2016-80875-C3-3-R, (Spanish Ministry of Science, Innovation and Universities); Author J.F.'s participation was supported by a Spanish Ministry of Sciences, Innovation and Universities Juan de la Cierva grant.

Conflict of Interest
The authors declare that there is no conflict of interest.

Acknowledgements

The authors are indebted to the Petrophysical Laboratory of IGEO, the group of Petrology applied to Heritage Conservation (921349). Thanks go as well to Non destructives techniques Service (MNCN), CAI of X-Ray diffraction-(UCM) and Carlos II University SEM Service (UC3M). Special thanks to Luis Alberto Rodriguez-Gomez for his advice and suggestions. .Mrs Margaret Clark is acknowledged for her assistance with English text. Special acknowledgements to the professional support of the Interdisciplinary Thematic Platform from CSIC, Open Heritage: Research and Society (PTI-PAIS).

Data Availability

The raw/processed data required to reproduce these findings cannot be shared at this time as the data also forms part of an ongoing study.

References

[1] S. Buys, V. Oakley, Conservation and Restoration of Ceramics, 2014. https://doi.org/10.4324/9780080502892.

[2] T.P. Santos, M. Fátima Vaz, M.L. Pinto, A.P. Carvalho, Porosity characterization of old Portuguese ceramic tiles, Constr. Build. Mater. 28 (2012) 104–110. https://doi.org/10.1016/j.conbuildmat.2011.08.004.

[3] RWW Rice, Comparison of stress concentration versus minimum solid area based mechanical property-porosity relations, J. Mater. Sci. (1993). https://doi.org/10.1007/BF00367582.

[4] R.M. Ion, I. Dumitriu, R.C. Fierascu, M.L. Ion, S.F. Pop, C. Radovici, R.I. Bunghez, V.I.R. Niculescu, Thermal and mineralogical investigations of historical ceramic: A case study, J. Therm. Anal. Calorim. 104 (2011) 487–493. https://doi.org/10.1007/s10973-011-1517-6.

[5] C. Di Benedetto, P. Cappelletti, M. Favaro, S.F. Graziano, A. Langella, D. Calcaterra, A. Colella, Porosity as key factor in the durability of two historical building stones: Neapolitan Yellow Tuff and Vicenza Stone, Eng. Geol. 193 (2015) 310–319. https://doi.org/10.1016/j.enggeo.2015.05.006.

[6] H.A. Viles, Durability and conservation of stone: Coping with complexity, Q. J. Eng. Geol. Hydrogeol. 46 (2013) 367–375. https://doi.org/10.1144/qjegh2012-053.

[7] F. Pino, P. Fermo, M. La Russa, S. Ruffolo, V. Comite, J. Baghdachi, E. Pecchioni, F. Fratini, G. Cappelletti, Advanced mortar coatings for cultural heritage protection. Durability towards prolonged UV and outdoor exposure, Environ. Sci. Pollut. Res. 24 (2017) 12608–12617. https://doi.org/10.1007/s11356-016-7611-3.

[8] E.T.G. Mibach, The restoration of coarse archaeological ceramics, Stud. Conserv. 20 (1975) 55–61. https://doi.org/10.1179/sic.1975.s1.010.

[9] E. Hansen, E. Doehne, J. Fidler, J. Larson, B. Martin, M. Matteini, C. Rodriguez-Navarro, E.S. Pardo, C. Price, A. de Tagle, J.M. Teutonico, N. Weiss, A review of selected inorganic consolidants and protective treatments for porous calcareous materials, Stud. Conserv. 48 (2003) 13–25. https://doi.org/10.1179/sic.2003.48.supplement-1.13.

[10] D. Benavente, M.A.G. del Cura, R. Fort, S. Ordónez, Durability estimation of porous building stones from pore structure and strength, Eng. Geol. 74 (2004) 113–127.

[11] L. Li, M. Aubertin, A general relationship between porosity and uniaxial strength of engineering materials, Can. J. Civ. Eng. (2003). https://doi.org/10.1139/l03-012.

[12] G. Carotenuto, G. Spagnuolo, L. Ambrosio, L. Nicolais, Macroporous hydroxyapatite as alloplastic material for dental applications, J. Mater. Sci. Mater. Med. 10 (1999) 671–676. https://doi.org/10.1023/a:1008952111545.

[13] T.J. Levingstone, S. Herbaj, N.J. Dunne, Calcium phosphate nanoparticles for therapeutic applications in bone regeneration, Nanomaterials. 9 (2019) 1570. https://doi.org/10.3390/nano9111570.

[14] E. Ruiz-Hitzky, P. Aranda, Novel architectures in porous materials based on clays, J. Sol-Gel Sci. Technol. 70 (2014) 307–316. https://doi.org/10.1007/s10971-013-3237-9.

[15] M. Steiger, A.E. Charola, K. Sterflinger, Weathering and deterioration, in: Stone Archit. Prop. Durab., 2011. https://doi.org/10.1007/978-3-642-14475-2_4.

[16] L.N.Y. Wong, V. Maruvanchery, G. Liu, Water effects on rock strength and stiffness degradation, Acta Geotech. 11 (2016) 713–737. https://doi.org/10.1007/s11440-015-0407-7.

[17] A.C. Lasaga, CHEMICAL KINETICS OF WATER-ROCK INTERACTIONS., in: J. Geophys. Res., 1984. https://doi.org/10.1029/jb089ib06p04009.

[18] Rabat, R. Tomás, M. Cano, T. Miranda, Impact of water on peak and residual shear strength parameters and triaxial deformability of high-porosity building calcarenite stones: Interconnection with their physical and petrological characteristics, Constr. Build. Mater. 262 (2020). https://doi.org/10.1016/j.conbuildmat.2020.120789.

[19] B. Vásárhelyi, Statistical analysis of the influence of water content on the strength of the miocene limestone, Rock Mech. Rock Eng. (2005). https://doi.org/10.1007/s00603-004-0034-3.

[20] W. Li, M. Pour-Ghaz, J. Castro, J. Weiss, Water Absorption and Critical Degree of Saturation Relating to Freeze-Thaw Damage in Concrete Pavement Joints, J. Mater. Civ. Eng. (2012). https://doi.org/10.1061/(asce)mt.1943-5533.0000383.

[21] C.M. Grossi, P. Brimblecombe, I. Harris, Predicting long term freeze-thaw risks on Europe built heritage and archaeological sites in a changing climate, Sci. Total Environ. (2007). https://doi.org/10.1016/j.scitotenv.2007.02.014.

[22] D. Camuffo, Acid rain and deterioration of monuments: How old is the phenomenon?, Atmos. Environ. Part B, Urban Atmos. 26 (1992) 241–247. https://doi.org/10.1016/0957-1272(92)90027-P.

[23] A.E. Charola, Salts in the Deterioration of Porous Materials: An Overview, J. Am. Inst.

Conserv. 39 (2000) 327–343. https://doi.org/10.2307/3179977.

[24] B. Lubelli, R.P.J. Van Hees, CJWP Groot, The role of sea salts in the occurrence of different damage mechanisms and decay patterns on brick masonry, in: Constr. Build. Mater., 2004. https://doi.org/10.1016/j.conbuildmat.2003.08.017.

[25] M.F. La Russa, S.A. Ruffolo, C.M. Belfiore, P. Aloise, L. Randazzo, N. Rovella, A. Pezzino, G. Montana, Study of the effects of salt crystallization on degradation of limestone rocks, Period. Di Mineral. 82 (2013). https://doi.org/10.2451/2013PM0007.

[26] D. Barca, V. Comite, C.M. Belfiore, A. Bonazza, M.F. La Russa, S.A. Ruffolo, G.M. Crisci, A. Pezzino, C. Sabbioni, Impact of air pollution in deterioration of carbonate building materials in Italian urban environments, Appl. Geochemistry. 48 (2014) 122–131. https://doi.org/10.1016/j.apgeochem.2014.07.002.

[27] E. Uchida, Y. Ogawa, N. Maeda, T. Nakagawa, Deterioration of stone materials in the Angkor Monuments, Cambodia, Dev. Geotech. Eng. 84 (2000) 329–340. https://doi.org/10.1016/S0165-1250(00)80027-9.

[28] G.W. Scherer, R. Flatt, G. Wheeler, Materials science research for the conservation of sculpture and monuments, MRS Bull. (2001). https://doi.org/10.1557/mrs2001.18.

[29] L.M.O. Sousa, L.M. Suárez del Río, L. Calleja, V.G. Ruiz de Argandoña, A. Rodríguez Rey, Influence of microfractures and porosity on the physico-mechanical properties and weathering of ornamental granites, Eng. Geol. (2005). https://doi.org/10.1016/j.enggeo.2004.10.001.

[30] A. Shortland, P. Degryse, Ceramics, Cambridge: Cambridge University Press, 2020.

[31] M. Matteini, Inorganic treatments for the consolidation and protection of stone artefacts and mural paintings, Conserv. Sci. Cult. Herit. 8 (2008) 13–27.

[32] A.P.F. Pinto, J.D. Rodrigues, Stone consolidation: The role of treatment procedures, J. Cult. Herit. 9 (2008) 38–53. https://doi.org/10.1016/j.culher.2007.06.004.

[33] M. Slavíková, F. Krejčí, J. Žemlička, M. Pech, P. Kotlík, J. Jakůbek, X-ray radiography and tomography for monitoring the penetration depth of consolidants in Opuka - the building stone of Prague monuments, J. Cult. Herit. (2012). https://doi.org/10.1016/j.culher.2012.01.010.

[34] M. Slavíková, F. Krejčí, P. Kotlík, J. Jakůbek, I. Tomandl, J. Vacík, Neutron and high-contrast X-ray micro-radiography as complementary tools for monitoring organosilicon consolidants in natural building stones, Nucl. Instruments Methods Phys. Res. Sect. B Beam Interact. with Mater. Atoms. (2014). https://doi.org/10.1016/j.nimb.2014.07.041.

[35] E. Franzoni, Rising damp removal from historical masonries: A still open challenge, Constr. Build. Mater. 54 (2014) 123–136. https://doi.org/10.1016/j.conbuildmat.2013.12.054.

[36] M. Balonis, Mineral Inorganic Treatments, in: Encycl. Archaeol. Sci., 2018: pp. 1–5. https://doi.org/10.1002/9781119188230.saseas0384.

[37] E. Possenti, C. Colombo, C. Conti, N. Marinoni, M. Merlini, R. Negrotti, M. Realini, G.D. Gatta, Consolidation of building materials with a phosphate-based treatment: Effects on the microstructure and on the 3D pore network, Mater. Charact. 154 (2019) 315–324. https://doi.org/10.1016/j.matchar.2019.05.037.

[38] X. Ma, M. Balonis, H. Pasco, M. Toumazou, D. Counts, I. Kakoulli, Evaluation of hydroxyapatite effects for the consolidation of a Hellenistic-Roman rock-cut chamber tomb at Athienou-Malloura in Cyprus, Constr. Build. Mater. 150 (2017) 333–344. https://doi.org/10.1016/j.conbuildmat.2017.06.012.

[39] E. Sassoni, S. Naidu, G.W. Scherer, The use of hydroxyapatite as a new inorganic consolidant for damaged carbonate stones, J. Cult. Herit. (2011). https://doi.org/10.1016/j.culher.2011.02.005.

[40] R.M. Ion, L. Iancu, G. Vasilievici, M.E. Grigore, R.E. Andrei, G.I. Radu, R.M. Grigorescu, S. Teodorescu, I.A. Bucurica, M.L. Ion, A.I. Gheboianu, C. Radulescu, I.D. Dulama, Ion-substituted carbonated hydroxyapatite coatings for model stone samples, Coatings. 9 (2019) 231. https://doi.org/10.3390/coatings9040231.

[41] R.M. Ion, D. Turcanu-Caruţiu, R.C. Fierəscu, I. Fierəscu, I.R. Bunghez, M.L. Ion, S. Teodorescu, G. Vasilievici, V. Rədiţoiu, Caoxite-hydroxyapatite composition as consolidating material for the chalk stone from Basarabi-Murfatlar churches ensemble, Appl. Surf. Sci. 358 (2015) 612–618. https://doi.org/10.1016/j.apsusc.2015.08.196.

[42] A. Murru, R. Fort, Diammonium hydrogen phosphate (DAP) as a consolidant in carbonate stones: Impact of application methods on effectiveness, J. Cult. Herit. 42 (2020) 45–55. https://doi.org/10.1016/j.culher.2019.09.003.

[43] L. Haurie, A.I. Fernández, J.I. Velasco, J.M. Chimenos, J.M.L. Cuesta, F. Espiell, Synthetic hydromagnesite as flame retardant. Evaluation of the flame behaviour in a polyethylene matrix, Polym. Degrad. Stab. 91 (2006) 989–994. https://doi.org/10.1016/j.polymdegradstab.2005.08.009.

[44] A. Burgos-Cara, C. V. Putnis, M. Ortega-Huertas, E. Ruiz-Agudo, Influence of pH and citrate on the formation of oxalate layers on calcite revealed by in situ nanoscale imaging, CrystEngComm. 19 (2017) 3420–3429. https://doi.org/10.1039/c7ce00305f.

[45] A. Burgos-Cara, E. Ruiz-Agudo, C. Rodriguez-Navarro, Effectiveness of oxalic acid treatments for the protection of marble surfaces, Mater. Des. (2017). https://doi.org/10.1016/j.matdes.2016.11.037.

[46] C. Vazquez-Calvo, M. Alvarez de Buergo, R. Fort, M.J. Varas, Characterization of patinas by means of microscopic techniques, Mater. Charact. 58 (2007) 1119–1132. https://doi.org/10.1016/j.matchar.2007.04.024.

[47] G. Bitossi, R. Giorgi, M. Mauro, B. Salvadori, L. Dei, Spectroscopic techniques in cultural heritage conservation: A survey, Appl. Spectrosc. Rev. 40 (2005) 187–228. https://doi.org/10.1081/ASR-200054370.

[48] L. Dei, B. Salvadori, Nanotechnology in cultural heritage conservation: nanometric slaked lime saves architectonic and artistic surfaces from decay, J. Cult. Herit. 7 (2006) 110–115. https://doi.org/10.1016/j.culher.2006.02.001.

[49] M.J. Mosquera, L.A.M. Carrascosa, N. Badreldin, Producing superhydrophobic/oleophobic coatings on Cultural Heritage building materials, Pure Appl. Chem. 90 (2018) 551–561. https://doi.org/10.1515/pac-2017-0404.

[50] I. de Rosario, T. Rivas, G. Buceta, J. Feijoo, M.J. Mosquera, Surfactant-Synthesized Consolidants Applied To A Granitic Medieval Necropolis In NW Spain. Laboratory And In Situ Effectiveness Evaluation, Int. J. Archit. Herit. 11 (2017) 1166–1176. https://doi.org/10.1080/15583058.2017.1354097.

[51] O. Chiantore, M. Lazzari, Photo-oxidative stability of paraloid acrylic protective polymers, Polymer (Guildf). (2001). https://doi.org/10.1016/S0032-3861(00)00327-X.

[52] E. Doehne, C.A. Price, Stone Conservation: An Overview of Current Research, 2nd edition, 2010. https://doi.org/10.1016/0006-3207(70)90031-5.

[53] L.S. Gomez-Villalba, P. López-Arce, M. Alvarez de Buergo, A. Zornoza-Indart, R. Fort, Mineralogical and textural considerations in the assessment of aesthetic changes in dolostones by effect of treatments with Ca(OH)2 nanoparticles, in: Sci. Technol. Conserv. Cult. Herit., 2013: p. 235. https://doi.org/10.1201/b15577.

[54] E. Franzoni, E. Rirsch, Y. Paselli, Which methods are suitable to assess the effectiveness of chemical injection treatments in the laboratory?, J. Build. Eng. 29 (2020). https://doi.org/10.1016/j.jobe.2019.101131.

[55] G. Chiari, Chemical surface treatments and capping techniques of earthen structures: a long term evaluation, in: 6th Int. Conf. Conserv. Earthen Archit. Adobe 90 Prepr. Las Cruces, New Mex. USSA, Oct. 14-19, 1990, 1990.

[56] I. Oztürk, Alkoxysilanes consolidation of stone and earthen building materials, (1992) 100p.

[57] M.J. Varas-Muriel, E.M. Pérez-Monserrat, C. Vázquez-Calvo, R. Fort, Effect of conservation treatments on heritage stone. Characterisation of decay processes in a case study, Constr. Build. Mater. 95 (2015) 611–622. https://doi.org/10.1016/j.conbuildmat.2015.07.087.

[58] M.E. David, R.M. Ion, R.M. Grigorescu, L. Iancu, E.R. Andrei, Nanomaterials used in conservation and restoration of cultural heritage: An up-to-date overview, Materials (Basel). 13 (2020) 2064. https://doi.org/10.3390/ma13092064.

[59] MFF La Russa, N. Rovella, M. Alvarez De Buergo, C.M. Belfiore, A. Pezzino, G.M. Crisci, S.A. Ruffolo, Nano-TiO2 coatings for cultural heritage protection: The role of the binder on hydrophobic and self-cleaning efficacy, Prog. Org. Coatings. 91 (2016) 1–8. https://doi.org/10.1016/j.porgcoat.2015.11.011.

[60] S. Tzavellos, G.L. Pesce, Y. Wu, A. Henry, S. Robson, R.J. Ball, Effectiveness of nanolime as a stone consolidant: A 4-year study of six common UK limestones, Materials (Basel). 12 (2019) 2673. https://doi.org/10.3390/ma12172673.

[61] P. López-Arce, L.S. Gomez-Villalba, L. Pinho, M.E. Fernández-Valle, M.Á. de Buergo, R. Fort, Influence of porosity and relative humidity on consolidation of dolostone with calcium hydroxide nanoparticles: Effectiveness assessment with non-destructive techniques, Mater. Charact. (2010). https://doi.org/10.1016/j.matchar.2009.11.007.

[62] A. Sierra-Fernandez, L.S. Gomez-Villalba, M.E. Rabanal, R. Fort, New nanomaterials for applications in conservation and restoration of stony materials: A review, Mater. Constr. (2017). https://doi.org/10.3989/mc.2017.07616.

[63] Y. Liu, J. Liu, Design of multifunctional SiO2–TiO2 composite coating materials for outdoor sandstone conservation, Ceram. Int. 42 (2016) 13470–13475. https://doi.org/10.1016/j.ceramint.2016.05.137.

[64] Y. Liu, Y. Shu, B. Sun, X. Zeng, J. Zhu, J. Yi, J. He, Electrochemical synthesis of In2O3 nanoparticles for fabricating ITO ceramics, Ceram. Int. 45 (2019) 19068–19076. https://doi.org/10.1016/j.ceramint.2019.06.151.

[65] G.H.A. Therese, P. V. Kamath, Electrochemical synthesis of metal oxides and hydroxides,

Chem. Mater. 12 (2000) 1195–1204. https://doi.org/10.1021/cm990447a.

[66] Z. Nagy, Electrochemical Synthesis of Inorganic Compounds: A Bibliography, 2013.

[67] H. Yang, J. Ouyang, A. Tang, Y. Xiao, X. Li, X. Dong, Y. Yu, Electrochemical synthesis and photocatalytic property of cuprous oxide nanoparticles, Mater. Res. Bull. 41 (2006) 1310–1318. https://doi.org/10.1016/j.materresbull.2006.01.004.

[68] P. Cassoux, L. Valade, P.L. Fabre, Electrochemical Methods, Electrocrystallization, in: Compr. Coord. Chem. II, 2004: pp. 761–773. https://doi.org/10.1016/B0-08-043748-6/01163-4.

[69] A. Doménech-Carbó, M.T. Doménech-Carbó, Electroanalytical techniques in archaeological and art conservation, Pure Appl. Chem. 90 (2018) 447–461. https://doi.org/10.1515/pac-2017-0508.

[70] E. Cano, B. Ramírez Barat, Electrochemical Techniques for in situ Corrosion Evaluation of Cultural Heritage, in: Adv. Charact. Tech. Diagnostic Tools Eval. Methods Herit. Sci., 2018: pp. 21–32. https://doi.org/10.1007/978-3-319-75316-4_2.

[71] L.M. Ottosen, C.M.D. Ferreira, I. V. Christensen, Electrokinetic desalination of glazed ceramic tiles, in: J. Appl. Electrochem., 2010: pp. 1161–1171. https://doi.org/10.1007/s10800-010-0086-x.

[72] E. Valentini, Smart electrochemical portable tools for cultural heritage analysis: A review, Sensors (Switzerland). 19 (2019) 4303. https://doi.org/10.3390/s19194303.

[73] A.M.R. Ramírez, M.A. Gacitúa, E. Ortega, F.R. Díaz, M.A. del Valle, Electrochemical in situ synthesis of polypyrrole nanowires, Electrochem. Commun. 102 (2019) 94–98. https://doi.org/10.1016/j.elecom.2019.04.007.

[74] Z. Zhao, R. Li, X. Zhang, C. Zhang, J. Liu, Y. Wang, Y. Wang, C. Fan, Electrochemical In-situ Synthesis and Photocatalytic Properties of BiF3 Thin Films, Gaodeng Xuexiao Huaxue Xuebao/Chemical J. Chinese Univ. (2018). https://doi.org/10.7503/cjcu20180001.

[75] R. Kataoka, M. Kitta, N. Takeichi, T. Kiyobayashi, Electrochemical In Situ Synthesis: A New Synthesis Route for Redox Active Manganese Oxides for Rechargeable Sodium Ion Battery through Initial Charge Process, J. Electrochem. Soc. 164 (2017) 226. https://doi.org/10.1149/2.0851702jes.

[76] S. Wustoni, T.C. Hidalgo, A. Hama, D. Ohayon, A. Savva, N. Wei, N. Wehbe, S. Inal, In Situ Electrochemical Synthesis of a Conducting Polymer Composite for Multimetabolite Sensing, Adv. Mater. Technol. 5 (2020) 1900943. https://doi.org/10.1002/admt.201900943.

[77] J. Feijoo, R. Fort, L.S. Gomez-Villalba, M.E. Rabanal, L.M. Ottosen, Electroprecipitation of Magnesium and Calcium Compounds for Weathering Protection of Ornamental Rocks, Cryst. Growth Des. 20 (2020) 2337–2355. https://doi.org/10.1021/acs.cgd.9b01497.

[78] J. Feijoo, X.R. Nóvoa, T. Rivas, Electrokinetic treatment to increase bearing capacity and durability of a granite, Mater. Struct. 50:251 (2017) 1–15. https://doi.org/https://doi.org/10.1617/s11527-017-1123-6.

[79] J. Feijoo, L.M. Ottosen, X.R. Nóvoa, T. Rivas, I. de Rosario, An improved electrokinetic method to consolidate porous materials, Mater. Struct. 50 (2017) 186. https://doi.org/10.1617/s11527-017-1063-1.

[80] J.W. Anthony, R.A. Bideaux, K.W. Bladh, M.C. Nichols., Handbook of Mineralogy, 2003.

[81] Webmineral, Mineralogy database, (n.d.) http://webmineral.com/.

[82] N. Tamura, P.U.P.A. Gilbert, X-ray microdiffraction of biominerals, Methods Enzymol. 532 (2013) 501–531. https://doi.org/10.1016/B978-0-12-416617-2.00021-7.

[83] O.H. Seeck, B. Murphy, X-ray diffraction: modern experimental techniques, 2015.

[84] R.T. Downs, M. Hall-Wallace, The American Mineralogist crystal structure database, Am. Mineral. 88 (2003) 247–250. https://doi.org/10.5860/choice.43sup-0302.

[85] G. Nichols, Applications of cathodoluminescence spectroscopy and imaging in the characterisation of pharmaceutical materials, Eur. J. Pharm. Sci. 45 (2012) 19–42. https://doi.org/10.1016/j.ejps.2011.10.017.

[86] S. Hildebrandt, J. Schreiber, W. Hergert, H. Uniewski, H.S. Leipner, Theoretical Fundamentals and Experimental Materials and Defect Studies Using Quantitative Scanning Electron Microscopy-Cathodoluminescence/electron Beam Induced Current on compound semiconductors, Scanning Microsc. 12 (1998) 535–552.

[87] F. Di Lorenzo, R.M. Rodríguez-Galán, M. Prieto, Kinetics of the solvent-mediated transformation of hydromagnesite into magnesite at different temperatures, Mineral. Mag. 78 (2014) 1363–1372. https://doi.org/10.1180/minmag.2014.078.6.02.

[88] A. Singh, A. Tiwari, J. Bajpai, AKK Bajpai, Biomaterials: From Action to Application, Handb. Antimicrob. Coatings. 27 (2017).

[89] M.A.S. Kalceff, M.R. Phillips, Cathodoluminescence microcharacterization of the defect structure of quartz, Phys. Rev. B. 52 (1995) 3122. https://doi.org/10.1103/PhysRevB.52.3122.

[90] M. Guzzi, M. Martini, M. Mattaini, F. Pio, G. Spinolo, Luminescence of fused silica: Observation of the O2- emission band, Phys. Rev. B. 35 (1987) 9407. https://doi.org/10.1103/PhysRevB.35.9407.

[91] C.M. MacRae, N.C. Wilson, A. Torpy, Hyperspectral cathodoluminescence, Mineral. Petrol. 107 (2013) 429–440. https://doi.org/10.1007/s00710-013-0272-8.

[92] J. Garcia-Guinea, L. Tormo, O. Azumendi, J. Ruiz, V. Correcher, Strong calcite-like spectra cathodoluminescence emission from allende meteorite CAI phases, Spectrosc. Lett. 44 (2011) 516–520. https://doi.org/10.1080/00387010.2011.610413.

[93] M.B. Toffolo, G. Ricci, L. Caneve, I. Kaplan-Ashiri, Luminescence reveals variations in local structural order of calcium carbonate polymorphs formed by different mechanisms, Sci. Rep. 9 (2019) 1–15. https://doi.org/10.1038/s41598-019-52587-7.

[94] R. Coy-Yll, T. Calderon, M. Aguilar, Thermoluminescence and radioluminescence in aragonite, Mineral. Petrol. 39 (1988) 39–53. https://doi.org/10.1007/BF01226261.

[95] N. Kusano, H. Nishido, K. Inoue, Cathodoluminescence of calcite decomposed from dolomite in high-temperature skarn, J. Mineral. Petrol. Sci. (2014). https://doi.org/10.2465/jmps.140612.

[96] M. Karakuş, R.E. Moore, CLM : A new technique for refractories, Am. Ceram. Soc. Bull. 77 (1998) 55–61.

[97] H. Gies, Zur Beziehung zwischen Photolumineszenz and Chemismus natürlicher Karbonate,

Neues Jahrb. Miner. Abh. 127 (1976) 1–46.

[98] C. Spotl, Cathodoluminescence of magnesite: examples from the eastern Alps, Geology. 19 (1991) 52–55. https://doi.org/10.1130/0091-7613(1991)019<0052:COMEFT>2.3.CO;2.

[99] Q. Li, Y. Ding, G. Yu, C. Li, F. Li, Y. Qian, Fabrication of light-emitting porous hydromagnesite with rosette-like architecture, Solid State Commun. 125 (2003) 117–120. https://doi.org/10.1016/S0038-1098(02)00710-X.

[100] J. Roman-Lopez, V. Correcher, J. Garcia-Guinea, P. Prado-Herrero, T. Rivera, I.B. Lozano, Effect of the chemical impurities on the luminescence emission of natural apatites, Spectrochim. Acta - Part A Mol. Biomol. Spectrosc. 126 (2014) 142–147. https://doi.org/10.1016/j.saa.2014.01.128.

[101] J. Götze, R.B. Heimann, H. Hildebrandt, U. Gburek, Microstructural investigation into calcium phosphate biomaterials by spatially resolved cathodoluminescence, Materwiss. Werksttech. 32 (2001) 130–136. https://doi.org/10.1002/1521-4052(200102)32:2<130::aid-mawe130>3.0.co;2-z.

[102] D. Habermann, J. Götze, R.D. Neuser, D.K. Richter, The phenomenon of intrinsic cathodoluminescence: Case studies of quartz, calcite and apatite, Zentralblatt Für Geol. Und Paläontologie Tl. 1. (1997) 1275–1284.

[103] C.M. MacRae, N.C. Wilson, Luminescence database I - Minerals and materials, Microsc. Microanal. 14 (2008) 184. https://doi.org/10.1017/S143192760808029X.

[104] D.L. Goloshchapov, D.A. Minakov, E.P. Domashevskaya, P. V. Seredin, Excitation of luminescence of the nanoporous bioactive nanocrystalline carbonate-substituted hydroxyapatite for early tooth disease detection, Results Phys. 7 (2017) 3853–3858. https://doi.org/10.1016/j.rinp.2017.09.055.

[105] BS. Gorobets, A.A. Rogojine, L. V Bershov, BS. Gorobets, A.A. Rogojine, LUMINESCENT SPECTRA OF MINERALS: REFERENCE-BOOK., Am. Mineral. (2004).

[106] V. Correcher, C. Briatte, C. Boronat, J. Garcia-Guinea, Radiation effect on cathodoluminescence and thermoluminescence emission of Ca-rich oxalates from the human body, Luminescence. 33 (2018) 1438–1444. https://doi.org/10.1002/bio.3571.

[107] D. Benavente, M.A. García del Cura, J. García-Guinea, S. Sánchez-Moral, S. Ordóñez, Role of pore structure in salt crystallisation in unsaturated porous stone, J. Cryst. Growth. 260 (2004) 532–544. https://doi.org/10.1016/j.jcrysgro.2003.09.004.

[108] A. Martín-Pérez, A. Alonso-Zarza, A. Iglesia, R. Martín-García, Do magnesian clays play a role in dolomite formation in alkaline environments? An example from Castañar Cave, Cáceres (Spain), Geogaceta. (2015) 15–18.

[109] L. Chou, R.M. Garrels, R. Wollast, Comparative study of the kinetics and mechanisms of dissolution of carbonate minerals, Chem. Geol. 78 (1989) 269–282. https://doi.org/10.1016/0009-2541(89)90063-6.

[110] L.N. Plummer, D.L. Parkhurst, T.M.L. Wigley, Critical review of the kinetics of calcite dissolution and precipitation, in: ACS Symp. Ser., 1979. https://doi.org/10.1021/bk-1979-0093.ch025.

[111] M. Apriani, W. Hadi, A. Masduqi, Synthesis of magnesium carbonate polymorphs from Indonesia traditional salt production wastewater, EnvironmentAsia. 11 (2018).

https://doi.org/10.14456/ea.2018.29.

[112] W.H. McComas, W. Rieman, The Effect of pH on the Solubility of Calcium Oxalate, J. Am. Chem. Soc. 64 (1942) 2948–2949. https://doi.org/10.1021/ja01264a061.

[113] BN. Bachra, precipitation of calcium carbonates and phosphates from metastable solutions, Ann. N. Y. Acad. Sci. 109 (1963) 251–255. https://doi.org/10.1111/j.1749-6632.1963.tb13469.x.

[114] V.N. Makarov, O.P. Korytnaya, A.S. Lugovskaya, T.N. Vasilieva, Effect of Particle Size on Solubility and Neutralizing Ability of Carbonate Minerals, Chem. Sustain. Devlopment. 11 (2003) 621–626.

[115] P. Patnaik, Handbook of Inorganic Chemicals McGraw-Hill Library of Congress Cataloging-in-Publication Data, 2003.

[116] P. Taylor, Solubility and stability of inorganic carbonates: an approach to the selection of waste form for carbon-14, (1987) 53.

[117] P. Somasundaran, D. Wang, Mineral-solution equilibria, Dev. Miner. Process. 17 (2006) 45–72. https://doi.org/10.1016/S0167-4528(06)17003-9.

[118] V.E. Badillo-Almaraz, J. Ly, Calcium sorption on hydroxyapatite in aqueous solutions: Reversible and nonreversible components, J. Colloid Interface Sci. 258 (2003) 27–32. https://doi.org/10.1016/S0021-9797(02)00178-9.

[119] K.H. Prakash, R. Kumar, C.P. Ooi, P. Cheang, KA Khor, Apparent solubility of hydroxyapatite in aqueous medium and its influence on the morphology of nanocrystallites with precipitation temperature, Langmuir. 22 (2006) 11002–11008. https://doi.org/10.1021/la0621665.

[120] H.B. Pan, B.W. Darvell, Calcium phosphate solubility: The need for re-evaluation, Cryst. Growth Des. 9 (2009) 639–645. https://doi.org/10.1021/cg801118v.

[121] P. Bénézeth, G.D. Saldi, J.L. Dandurand, J. Schott, Experimental determination of the solubility product of magnesite at 50 to 200°C, Chem. Geol. 286 (2011) 21–31. https://doi.org/10.1016/j.chemgeo.2011.04.016.

[122] P. Grøn, M. Spinelli, O. Trautz, F. Brudevold, The effect of carbonate on the solubility of hydroxylapatite, Arch. Oral Biol. 8 (1963) 251–263. https://doi.org/10.1016/0003-9969(63)90016-5.

[123] J. Toulouse, Effect of point defects and disorder on structural phase transitions, 1997.

[124] E. Ruiz-Agudo, C. V. Putnis, A. Putnis, Coupled dissolution and precipitation at mineral-fluid interfaces, Chem. Geol. 383 (2014) 132–146. https://doi.org/10.1016/j.chemgeo.2014.06.007.

[125] I.M. Power, A.L. Harrison, G.M. Dipple, S.A. Wilson, P.B. Kelemen, M. Hitch, G. Southam, Carbon mineralization: From natural analogues to engineered systems, Rev. Mineral. Geochemistry. 77 (2013) 305–360. https://doi.org/10.2138/rmg.2013.77.9.

[126] R.M. Espinosa-Marzal, G.W. Scherer, Impact of in-pore salt scrystallisation on transport properties, Environ. Earth Sci. 69 (2013) 2657–2669. https://doi.org/10.1007/s12665-012-2087-z.

[127] L.S. Gomez-Villalba, P. López-Arce, M. Alvarez De Buergo, R. Fort, Atomic defects and

their relationship to aragonite-calcite transformation in portlandite nanocrystal carbonation, Cryst. Growth Des. 12 (2012) 4844–4852. https://doi.org/10.1021/cg300628m.

[128] Q. Gautier, P. Bénézeth, V. Mavromatis, J. Schott, Hydromagnesite solubility product and growth kinetics in aqueous solution from 25 to 75°C, Geochim. Cosmochim. Acta. 138 (2014) 1–20. https://doi.org/10.1016/j.gca.2014.03.044.

[129] P. Benezeth, Q. Gautier, N. Berninger, T. Roncal-herrero, R. KröGER, D. Alloyeau, V. Mavromatis, B. Purgstaller, J. Schott, Magnesium carbonate bearing minerals – Macroscopic to nano scale experimental data and observations, Goldschmidt. (2016) 2–3.

[130] J.K. Moore, J.A. Surface, A. Brenner, P. Skemer, M.S. Conradi, S.E. Hayes, Quantitative identification of metastable magnesium carbonate minerals by solid-state 13C NMR spectroscopy, Environ. Sci. Technol. 49 (2015) 657–664. https://doi.org/10.1021/es503390d.

[131] Z. Zhang, Y. Zheng, Y. Ni, Z. Liu, J. Chen, X. Liang, Temperature- And pH-dependent morphology and FT-IR analysis of magnesium carbonate hydrates, J. Phys. Chem. B. 110 (2006) 12969–12973. https://doi.org/10.1021/jp061261j.

[132] O. Mekmene, S. Quillard, T. Rouillon, J.M. Bouler, M. Piot, F. Gaucheron, Effects of pH and Ca/P molar ratio on the quantity and crystalline structure of calcium phosphates obtained from aqueous solutions, Dairy Sci. Technol. 89 (2009) 301–316. https://doi.org/10.1051/dst/2009019.

[133] M.S. Tung, Calcium Phosphates: Structure, Composition, Solubility, and Stability, in: Calcium Phosphates Biol. Ind. Syst., 1998: pp. 1–19. https://doi.org/10.1007/978-1-4615-5517-9_1.

[134] J. Zeglinski, M. Nolan, D. Thompson, S.A.M. Tofail, Reassigning the most stable surface of hydroxyapatite to the water resistant hydroxyl terminated (010) surface, Surf. Sci. 623 (2014) 55–63. https://doi.org/10.1016/j.susc.2014.01.008.

[135] R.G. Carrodeguas, S. De Aza, α-Tricalcium phosphate: Synthesis, properties and biomedical applications, Acta Biomater. 7 (2011) 3536–3546. https://doi.org/10.1016/j.actbio.2011.06.019.

[136] S. Fiore, R. Laviano, Brushite, hydroxylapatite, and taranakite from Apulian caves (southern Italy): New mineralogical data, Am. Mineral. 76 (1991) 1722–1727.

[137] M. Tanahashi, K. Kamiya, T. Suzuki, H. Nasu, Fibrous hydroxyapatite grown in the gel system: effects of pH of the solution on the growth rate and morphology, J. Mater. Sci. Mater. Med. 3 (1992) 48–53. https://doi.org/10.1007/BF00702944.

[138] E. Fujii, K. Kawabata, Y. Shirosaki, S. Hayakawa, A. Osaka, Fabrication of calcium phosphate nanoparticles in a continuous flow tube reactor, J. Ceram. Soc. Japan. 123 (2015) 101–105. https://doi.org/10.2109/jcersj2.123.101.

[139] P.G. Koutsoukos, Influence of Metal Ions on the Crystal Growth of Calcium Phosphates, Calcium Phosphates Biol. Ind. Syst. (1998). https://doi.org/https://doi.org/10.1007/978-1-4615-5517-9_7.

[140] Y.W. Wang, H.K. Christenson, F.C. Meldrum, Confinement increases the lifetimes of hydroxyapatite precursors, Chem. Mater. 26 (2014) 5830–5838. https://doi.org/10.1021/cm501770r.

[141] T. Toshima, R. Hamai, M. Tafu, Y. Takemura, S. Fujita, T. Chohji, S. Tanda, S. Li, G.W.

Qin, Morphology control of brushite prepared by aqueous solution synthesis, J. Asian Ceram. Soc. 2 (2014) 52–56. https://doi.org/10.1016/j.jascer.2014.01.004.

[142] L. Brečević, D. Škrtić, J. Garside, Transformation of calcium oxalate hydrates, J. Cryst. Growth. 74 (1986) 399–408. https://doi.org/10.1016/0022-0248(86)90131-4.

[143] F.T. Mackenzie, A. Lerman, Mineralogy, Chemistry, and Reaction Kinetics of the Major Carbonate Phases, in: Carbon Geobiosph. — Earth's Outer Shell —, 2006: pp. 89–121. https://doi.org/10.1007/1-4020-4238-8_4.

[144] G.M. Gadd, Fungal production of citric and oxalic acid: Importance in metal speciation, physiology and biogeochemical processes, Adv. Microb. Physiol. 41 (1999) 47–92. https://doi.org/10.1016/s0065-2911(08)60165-4.

[145] M.A. Larson, D.C. Timm, P.R. Wolff, Effect of suspension density on crystal size distribution, AIChE J. 14 (n.d.) 448–452. https://doi.org/https://doi.org/10.1002/aic.690140320.

Fig. 1. Untreated sandstone: a) sandstone texture showing intergranular porosity (blue), quartz (Qz) and kaolinite (K) (PLOM, parallel nicols image); b) original texture, inter-granular porosity (dark grey) and partially clay mineral-filled pores (SEM/BSE image); c) low magnification SEM/BSE image showing the porosity between quartz grains; d) inter-granular porosity details (processed image); e) roughness intensity profile of inter-granular porosity in the cross-section defined by the dotted line in Fig. 1c); f) XRD pattern; g) ESEM-cathodoluminescence spectrum.

Fig. 2. calcium carbonate treatment: a) fibrous calcium carbonate crystallisation (Cc) in sandstone, inter-granular porosity (blue), quartz (Qz), kaolinite (K) and titanium oxides (Ti), (PLOM, parallel nicols image); b and c) neo-formed aragonite (Ar) calcite (calc) crystals and amorphous carbonate (ACC) (SEM/SE image); d) aragonite growing in a pore between quartz and occasional calcite crystals (calc); d), inter-granular (green) and intercrystalline (red) porosity (processed image); e) roughness intensity profile of inter-granular and intercrystalline porosity in the cross-section defined by the dotted line in Fig. 2c.

Fig. 3. a) Aragonite (Ar) and calcite (Calc) porosity and in-pore growth details: (SEM/BSE image); b) quartz (Qz), aragonite (Ar) and calcite (Calc) (processed image); c) honeycomb texture developed by aragonite inside a pore, indicating secondary intercrystalline porosity (SEM/SE image); d) calcium carbonate (Cc) inter-growth in areas containing kaolinite (K) (SEM/BSE image).

Fig. 4. a) X-ray microdiffraction pattern of mineralisation in calcium carbonate treatment; b) cathodoluminescence spectrum for the band in the λ=300 nm to 400 nm region; c) EDS findings, positioning calcium carbonate polymorphs on the Ca/O/C ternary diagram

Fig. 5. Magnesium carbonate treatment: a) hydromagnesite crystallisation (HM), inter-granular porosity (blue), quartz (Qz) and kaolinite (K) (PLOM-parallel nicols); b) neo-formed HM crystals and magnesite (M) (SEM/SE image); c) HM growth in pores in the quartz inter-granular space(SEM/BSE); d) processed image highlighting details of inter-granular and intercrystalline porosity; e) roughness intensity profile describing inter-granular and intercrystalline porosity in the cross-section defined by the dotted line in Fig. 5c.

Fig. 6. Detailed views of: a) hydromagnesite (HM) filling the quartz (Qz) intergranular space; and b) magnesium carbonate dissolution and reprecipitation in pores (SEM/SE images).

Fig. 7. a) X-ray microdiffraction pattern of mineralisation in magnesium carbonate treatment; b) cathodoluminescence spectrum for the band in the λ=300 nm to 500 nm region; c) EDS chemical analyses, positioning magnesite and hydromagnesite on the Mg/O/C ternary diagram.

Fig. 8. Calcium phosphate treatment: a) calcium phosphate crystallisation (brown), inter-granular porosity (blue), quartz (Qz) and kaolinite- (K) (PLOM-parallel nicols image); b) showing hydroxyapatite plates (HAP) filling a pore (SEM/SE image); c) HAP growth in pores in the quartz inter-granular space, and direction of HAP fibre growth (SEM/BSE); d) processed image highlighting details of inter-granular and intercrystalline porosity.

Fig. 9. Porosity in sandstone treated with calcium phosphate, details: a) HAP crystals filling the space between quartz (Qz) grains (SEM/BSE); b) inter-granular porosity (green) and intercrystalline neo-porosity (red); c) roughness intensity profile showing the two types of porosity in the cross-section defined by the dotted line in Fig. 9a; d) petal-like dicalcium phosphate dihydrate (DCPD, brushite) crystals giving place to intercrystalline porosity.

Fig. 10. a) X-ray microdiffraction pattern of mineralisation in calcium phosphate treatment; b) cathodoluminescence spectrum for the band in the λ=300 nm to 500 nm region; c) EDS findings, positioning calcium phosphate polymorphs on the P/O/C ternary diagram.

Fig. 11. Electro-precipitation with calcium oxalate: a) calcium oxalate crystallisation (C-ox), inter-granular porosity (blue), quartz (Qz) and kaolinite-like phyllosilicates (K) (PLOM-parallel nicols image); b) neo-formed whewellite crystals (C-Ox) (SEM/SE image); c) whewellite growth in pores in the quartz inter-granular space (SEM/BSE image); d) details of inter-granular and intercrystalline porosity(processed image); e) roughness intensity profile showing inter-granular and intercrystalline porosity in the cross-section defined by the dotted line in Fig. 11c .

Fig. 12. a) Whewellite dissolution after precipitation; b) dissolution details from the selected area in Fig. 12a at higher magnification (SEM/SE images).

Fig. 13. a) X-ray microdiffraction pattern of mineralisation in calcium oxalate treatment; b) cathodoluminescence spectrum for the band in the λ=300 nm to 500 nm region; c) EDS findings, positioning calcium oxalate polymorphs on the Ca/O/C ternary diagram.

Fig. 14. SEM images processed to highlight textural details, neo-mineralisation positions and orientation and pore areas (green) in: a) untreated sandstone; and stone treated with b) calcium carbonate; c) magnesium carbonate; d) calcium phosphate; and e) calcium oxalate (porosity value given in respective legends; abbreviations: quartz (Qz), kaolinite-like clay minerals (K), aragonite (Ar), hydromagnesite (HM), hydroxyapatite (HAP) and whewellite (C-Ox).

Fig.15. a) Comparison of results of treatments and their effect on calculated inter-granular and intercrystalline porosity (in per cent of area); b) filled/unfilled pore ratio; c) percentage of total surface occupied, by treatment; d) mean inter-granular pore length and width (μm) , e and f) comparison of particle size in the neo-crystallised phases based on SEM imaging: e) length; f) width.

Figure 1

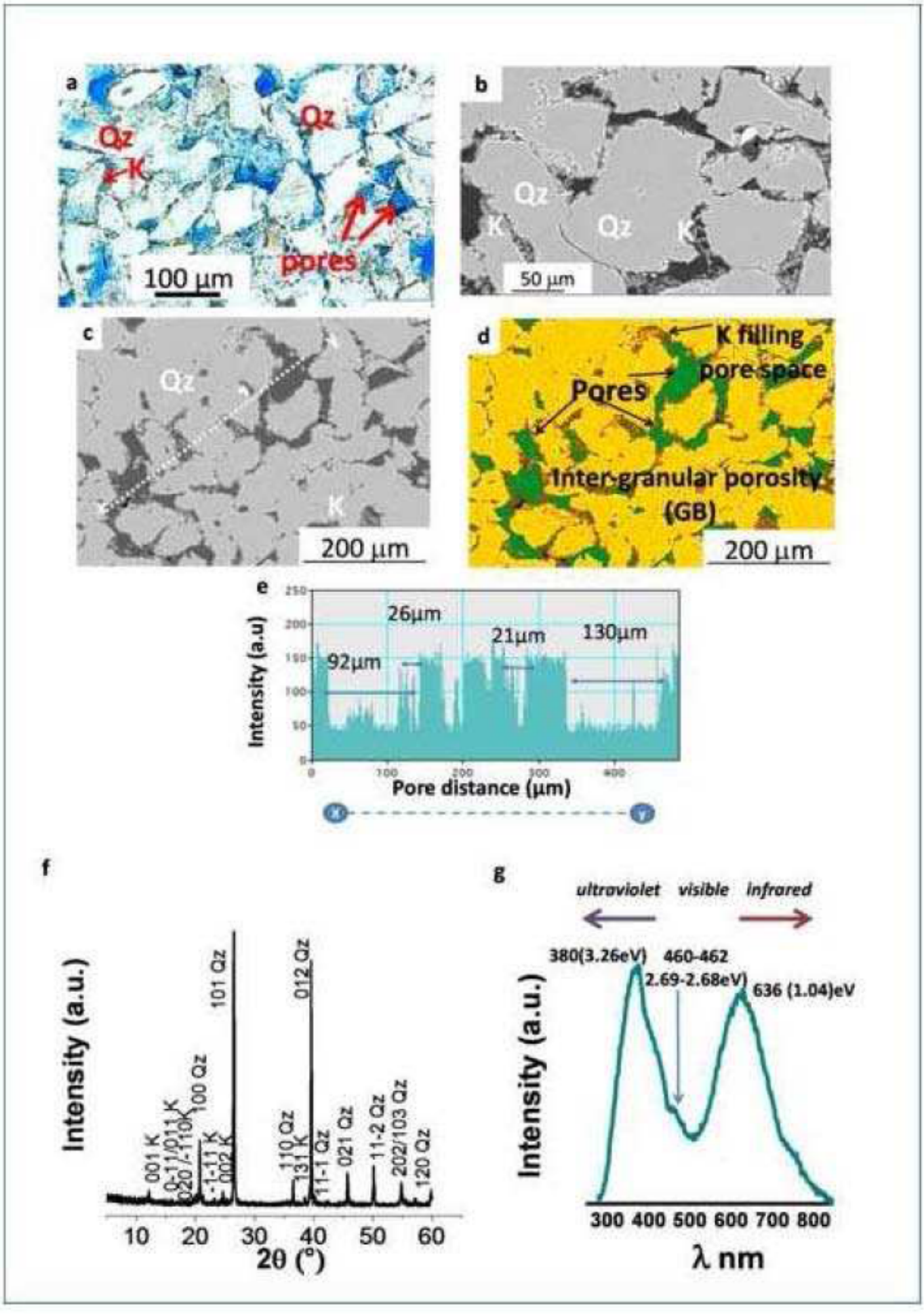
a
Qz
K
Qz
pores
100 µm
b
Qz
K
Qz
K
50 µm
c
Qz
K
200 µm
d
K filling
pore space
Pores
Inter-granular porosity
(GB)
200 µm
e
Intensity (a.u)
26µm
92µm
21µm
130µm
Pore distance (µm)
f
Intensity (a.u.)
001 K
0-11/011 K
020/110 K
100 Qz
1-11 K
002 K
101 Qz
110 Qz
131 K
11-1 Qz
012 Qz
021 Qz
11-2 Qz
202/103 Qz
120 Qz
10 20 30 40 50 60
2θ (°)
g
ultraviolet
visible
infrared
380(3.26eV)
460-462
2.69-2.68eV)
636 (1.04)eV
Intensity (a.u.)
300 400 500 600 700 800
λ nm

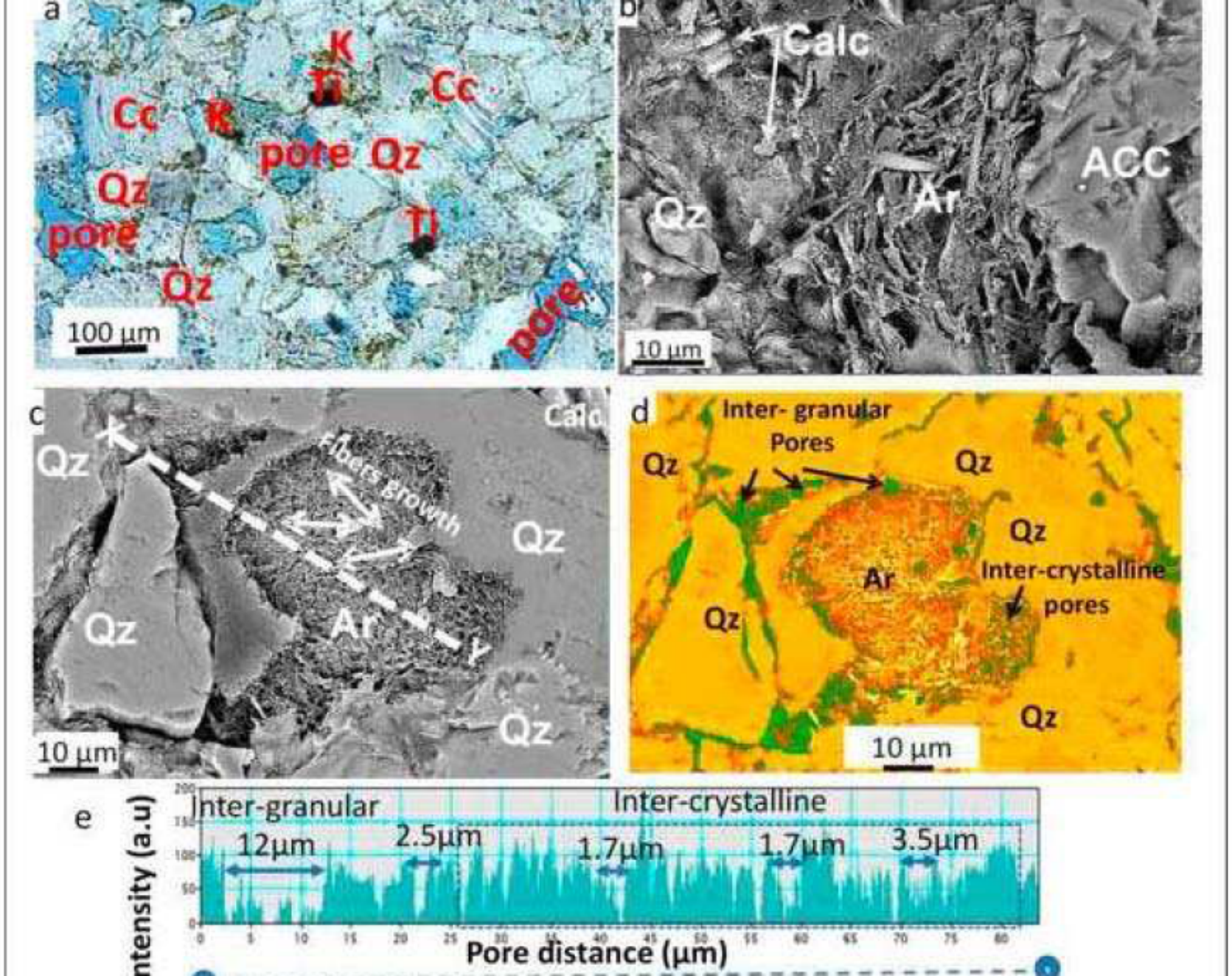
a
K
Ti
Cc
Cc
K
pore
Qz
Qz
pore
Ti
Qz
pore
100 µm
b
Calc
ACC
Ar
Qz
10 µm
c
Calc
Qz
Fibers growth
Qz
Ar
Qz
Qz
10 µm
d
Inter- granular
Pores
Qz
Qz
Qz
Ar
Inter-crystalline
pores
Qz
Qz
10 µm
e
Inter-granular
Inter-crystalline
12µm
2.5µm
1.7µm
1.7µm
3.5µm
Intensity (a.u)
Pore distance (µm)

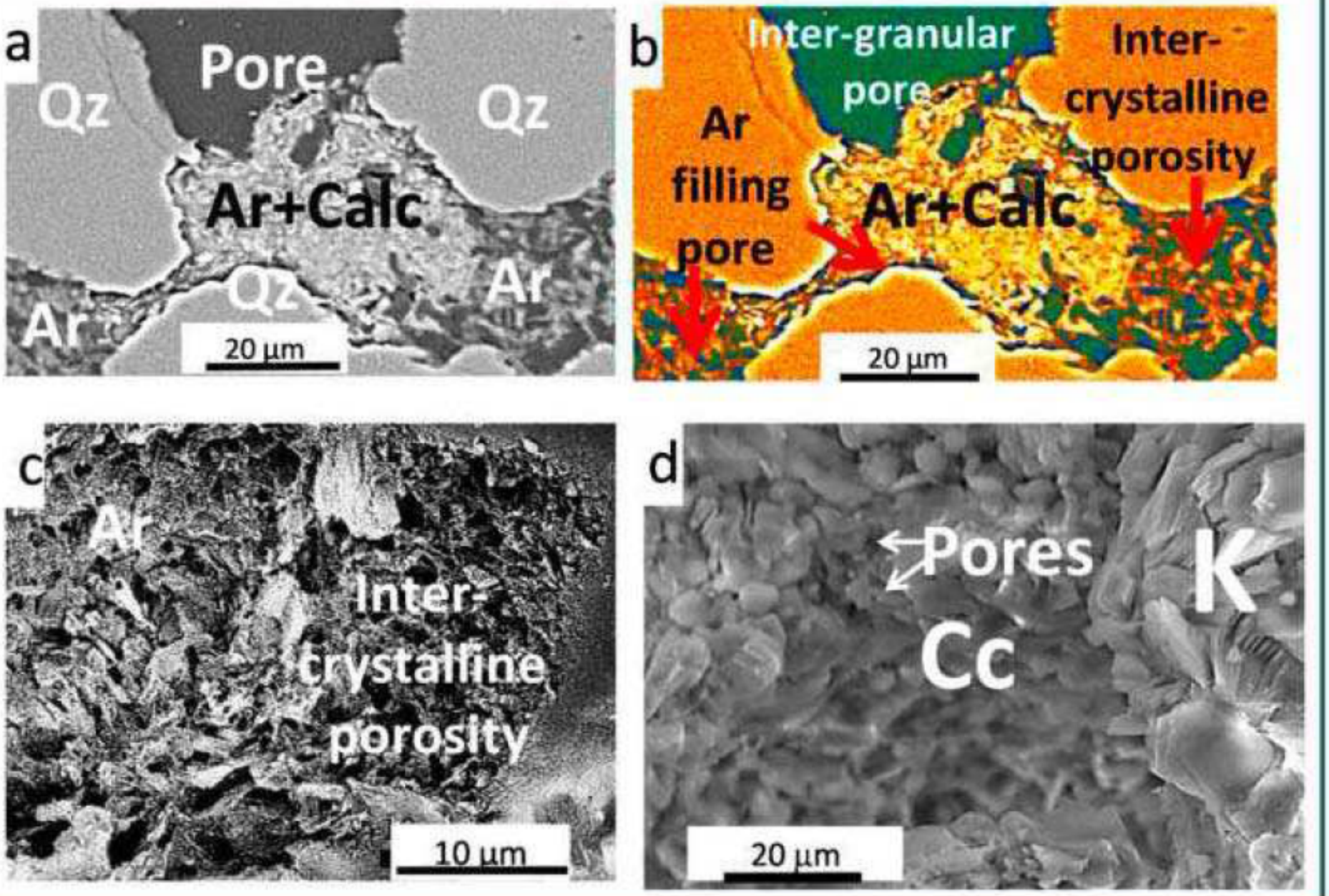
a
Pore
Qz
Qz
Ar+Calc
Qz
Ar
Ar
20 µm
b
Inter-granular pore
Inter-crystalline porosity
Ar filling pore
Ar+Calc
20 µm
c
Ar
Inter-crystalline porosity
10 µm
d
Pores
K
Cc
20 µm

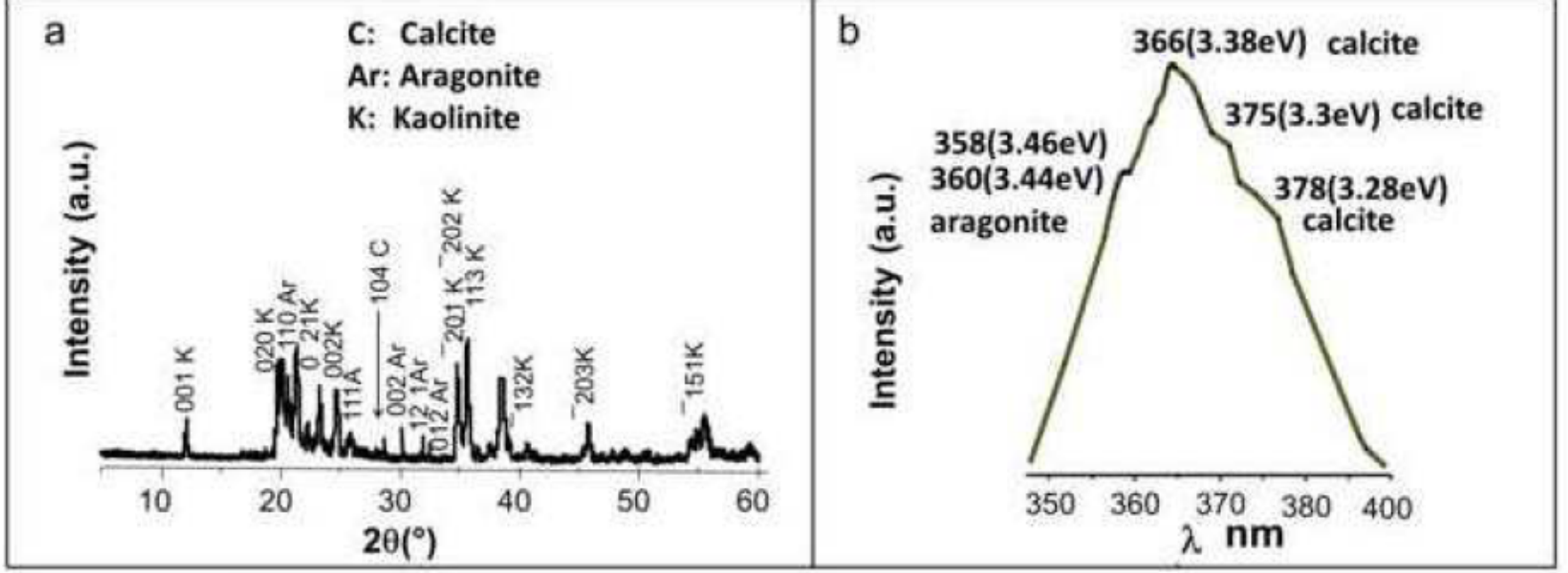

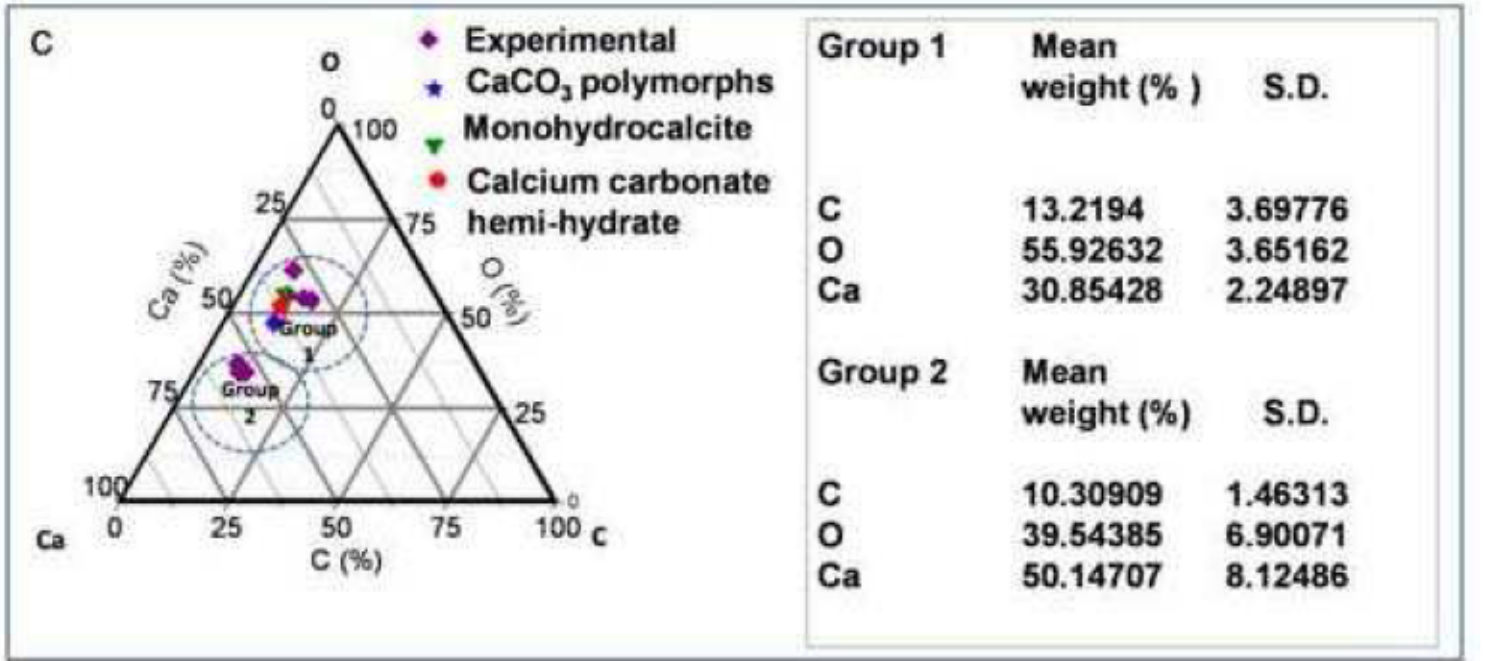

Group 1	Mean weight (%)	S.D.
C	13.2194	3.69776
O	55.92632	3.65162
Ca	30.85428	2.24897
Group 2	**Mean weight (%)**	**S.D.**
C	10.30909	1.46313
O	39.54385	6.90071
Ca	50.14707	8.12486

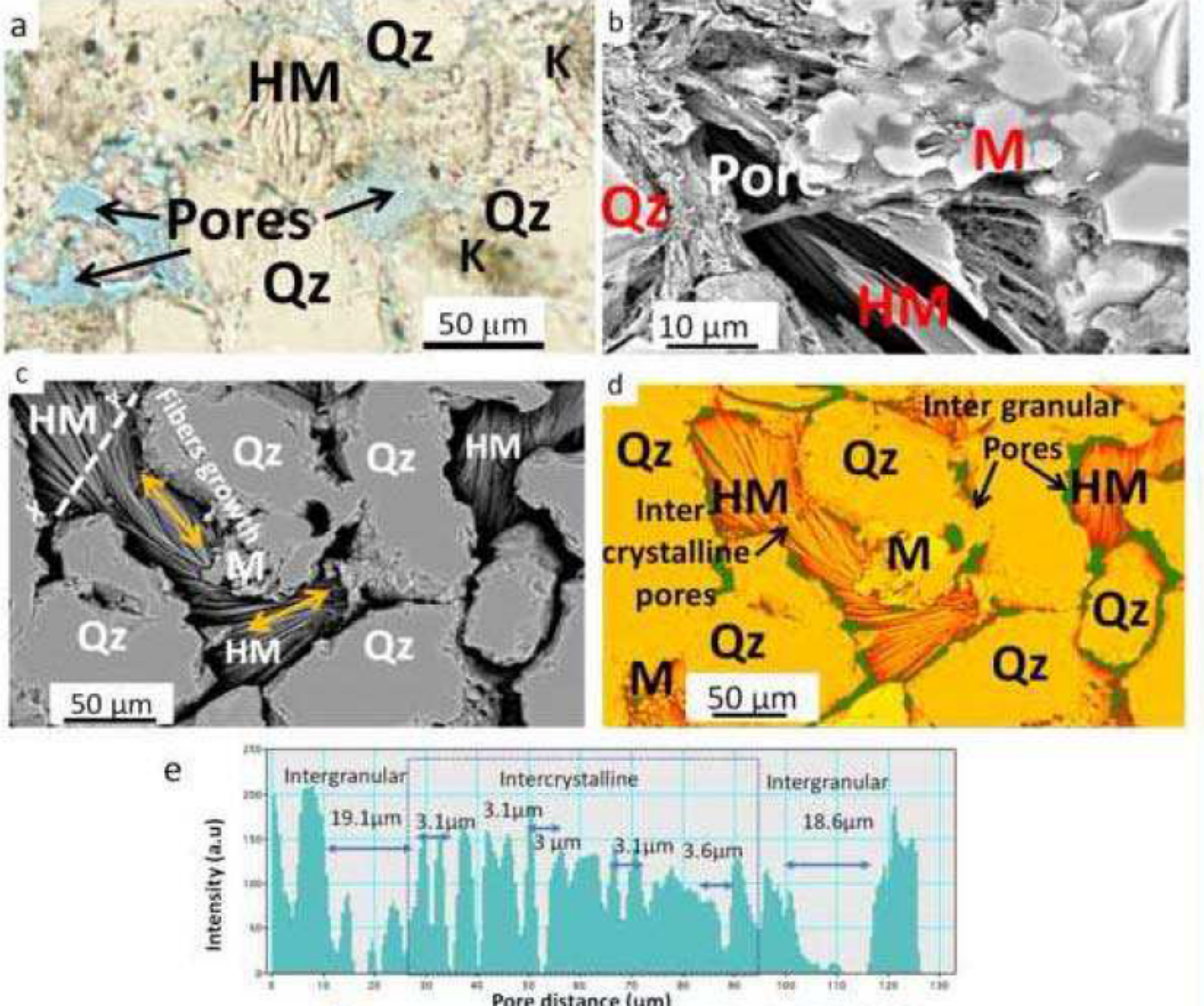
a
HM
Qz
K
Pores
Qz
K
Qz
50 µm
b
Qz
Por
M
HM
10 µm
c
HM
Fibers growth
Qz
Qz
HM
M
Qz
HM
Qz
50 µm
d
Inter granular
Pores
Qz
Qz
HM
HM
Inter
crystalline
pores
M
Qz
Qz
Qz
M
50 µm
e
Intergranular
Intercrystalline
Intergranular
19.1µm
3.1µm
3.1µm
3 µm
3.1µm
3.6µm
18.6µm
Intensity (a.u)
Pore distance (µm)

Figure 6

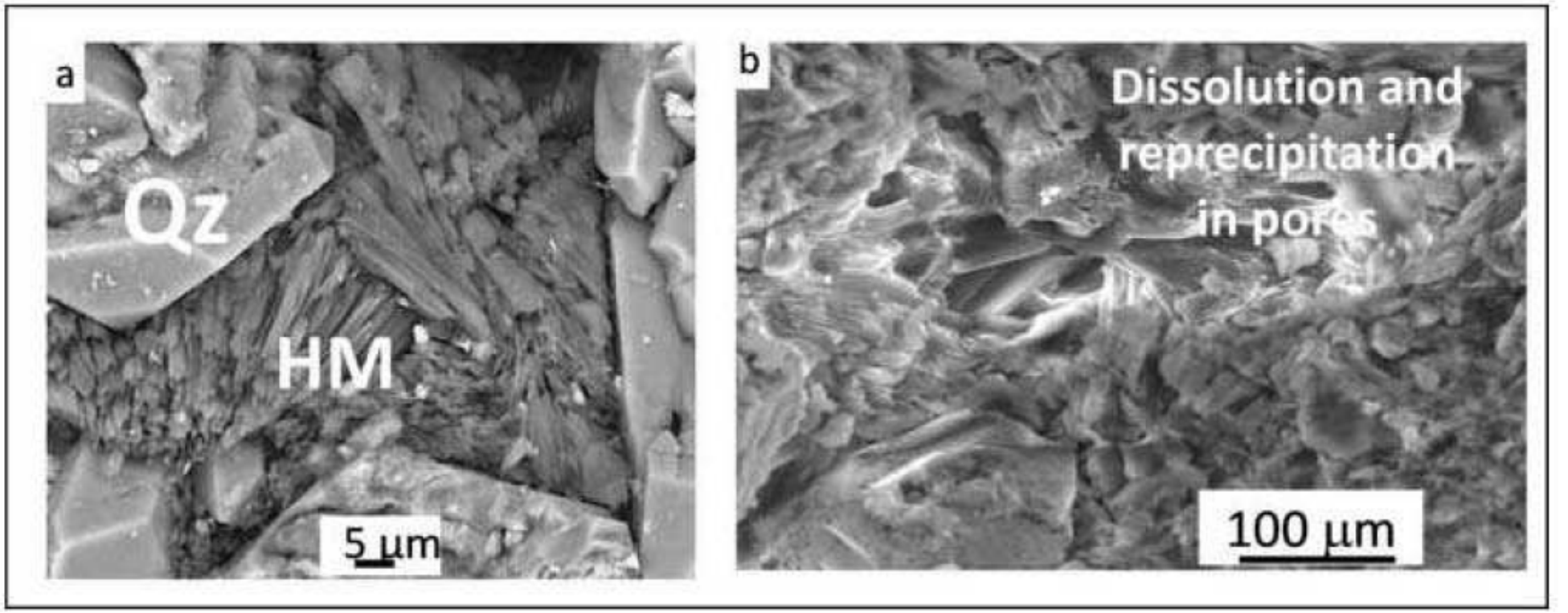
a
Qz
HM
5 µm
b
Dissolution and reprecipitation in pores
100 µm

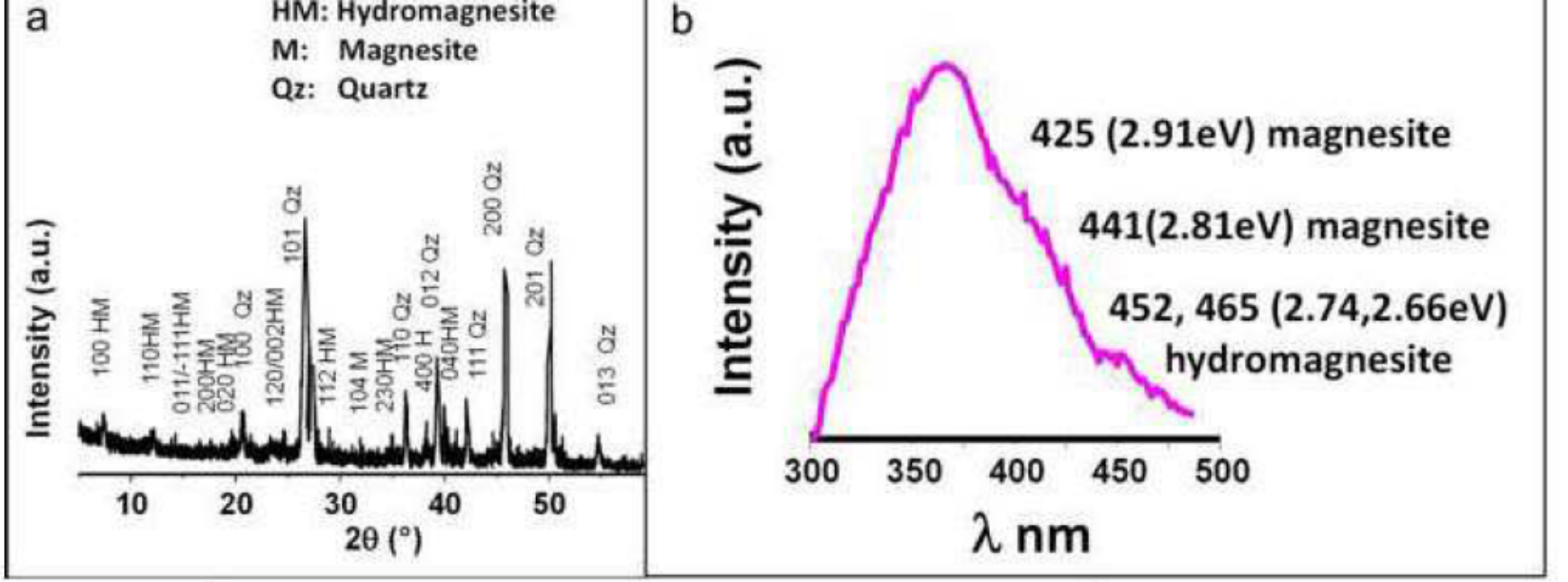

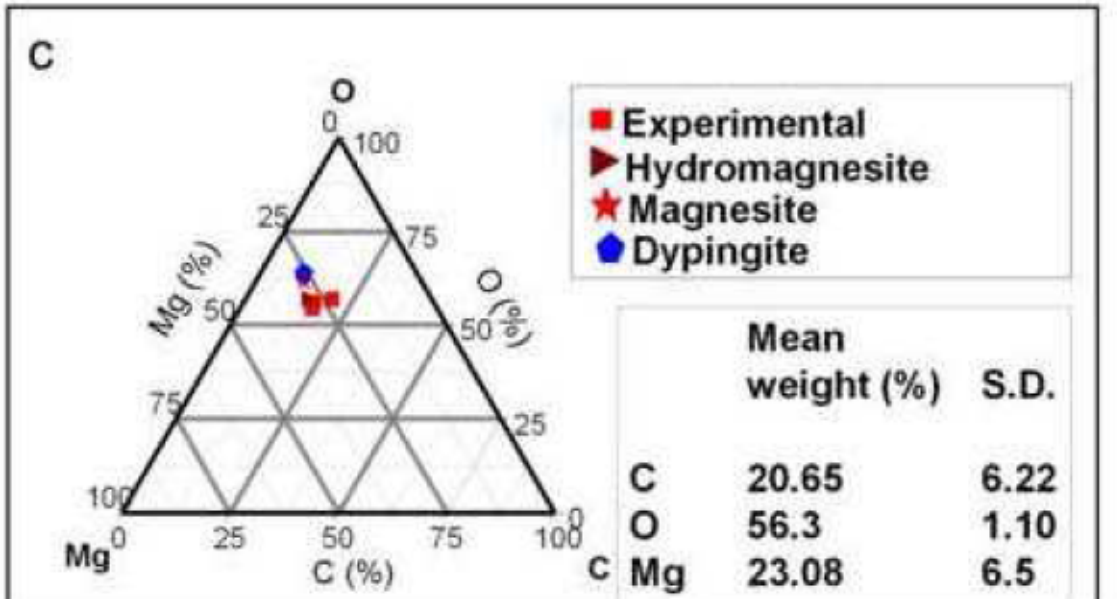

	Mean weight (%)	S.D.
C	20.65	6.22
O	56.3	1.10
Mg	23.08	6.5

Figure 8

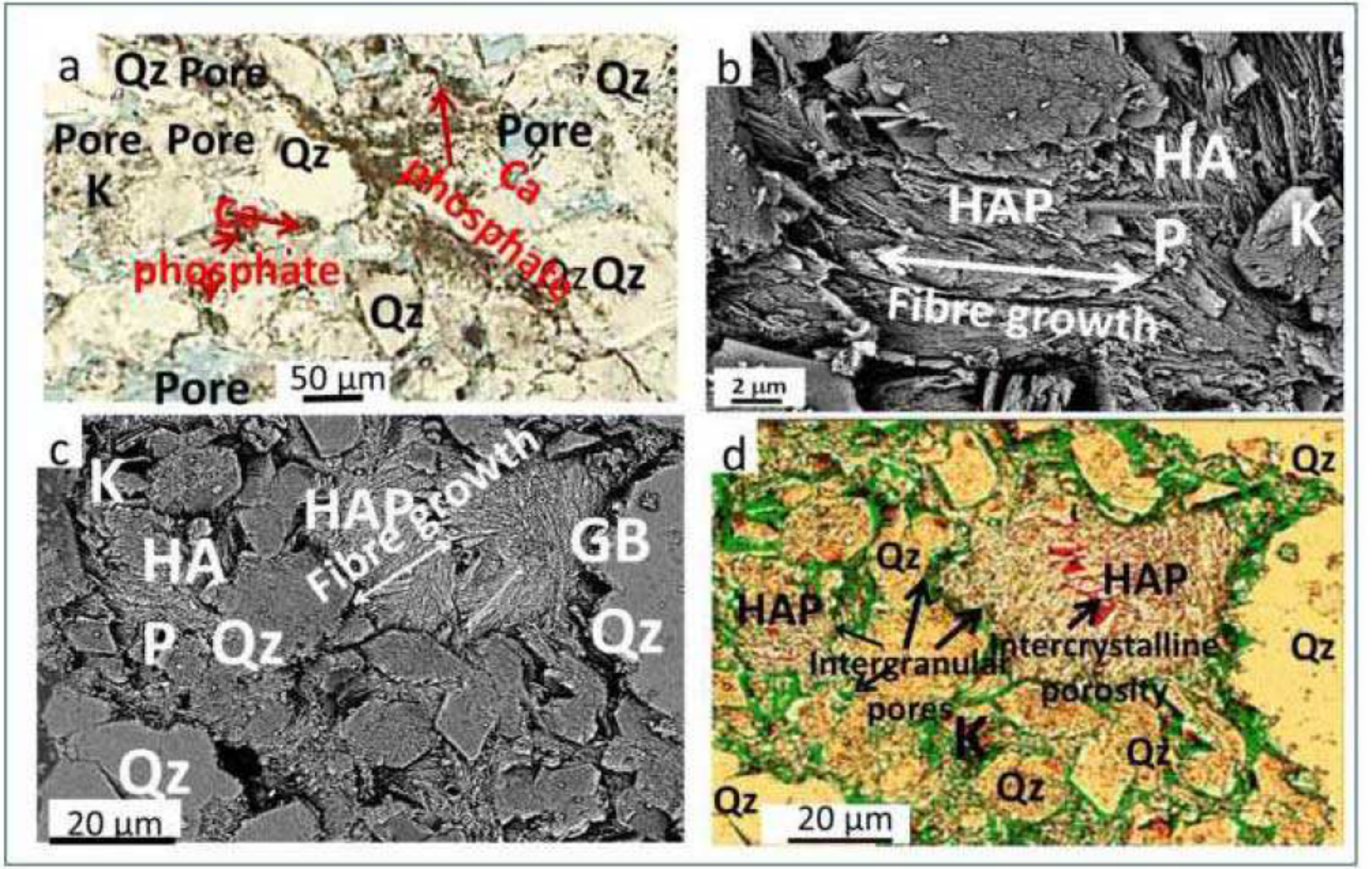
a
Qz Pore
Qz
Pore Pore
Qz
Pore
K
Ca phosphate
Ca phosphate
Qz Qz
Qz
Pore
50 µm
b
HA
HAP
P
K
Fibre growth
2 µm
c
K
HAP
Fibre growth
HA
GB
P
Qz
Qz
Qz
20 µm
d
Qz
Qz
HAP
HAP
Intergranular pores
Intercrystalline porosity
Qz
K
Qz
Qz
Qz
20 µm

Figure 9

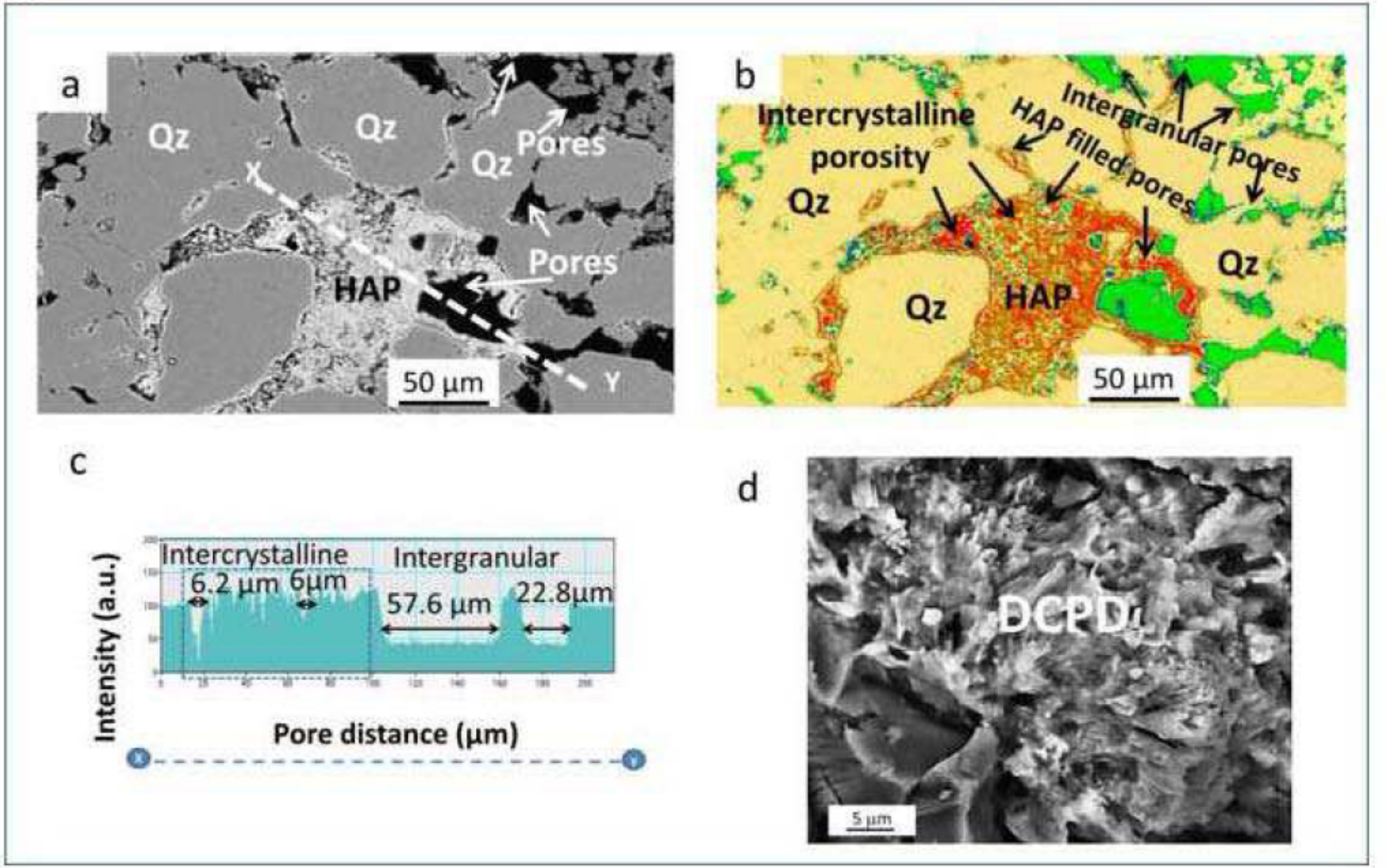
a
Qz
Qz
Qz
Pores
X
Pores
HAP
50 µm
Y
b
Intercrystalline
porosity
HAP filled pores
Intergranular pores
Qz
Qz
HAP
Qz
50 µm
c
Intercrystalline
Intergranular
6.2 µm
6µm
57.6 µm
22.8µm
Intensity (a.u.)
Pore distance (µm)
d
DCPD
5 µm

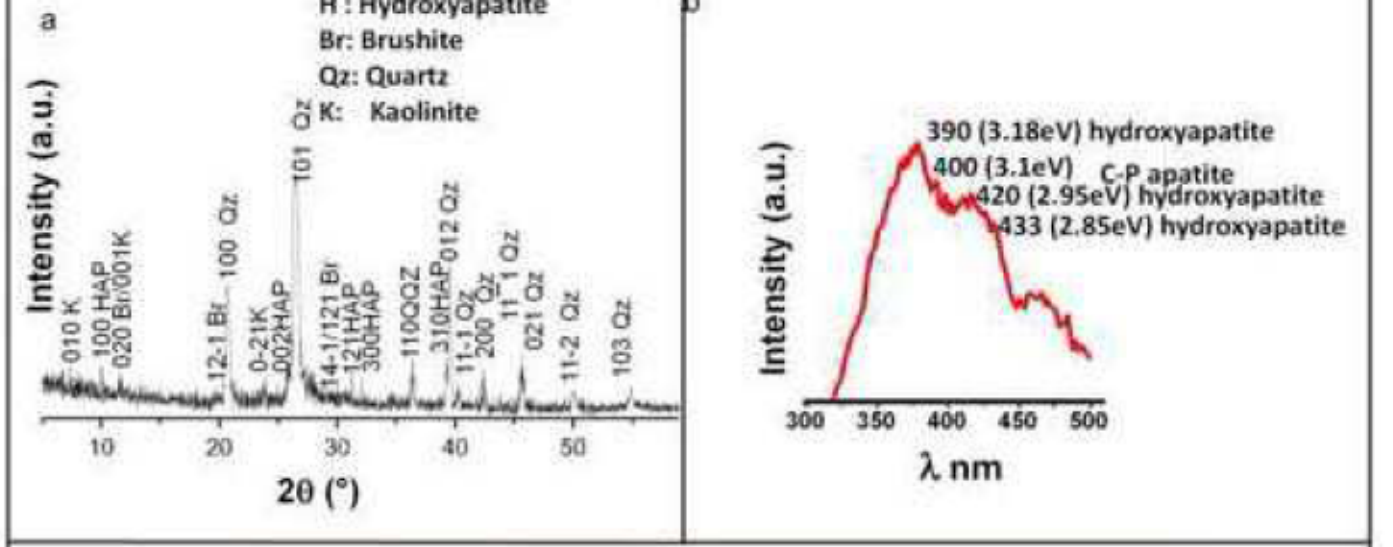

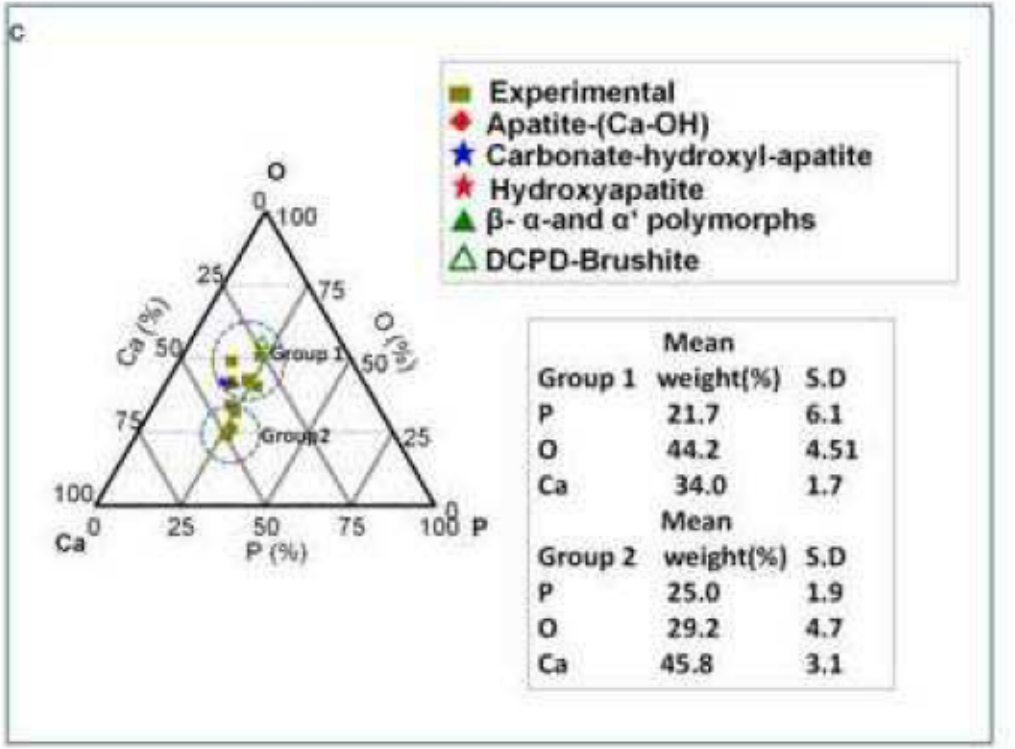

Group 1	Mean weight(%)	S.D
P	21.7	6.1
O	44.2	4.51
Ca	34.0	1.7

Group 2	Mean weight(%)	S.D
P	25.0	1.9
O	29.2	4.7
Ca	45.8	3.1

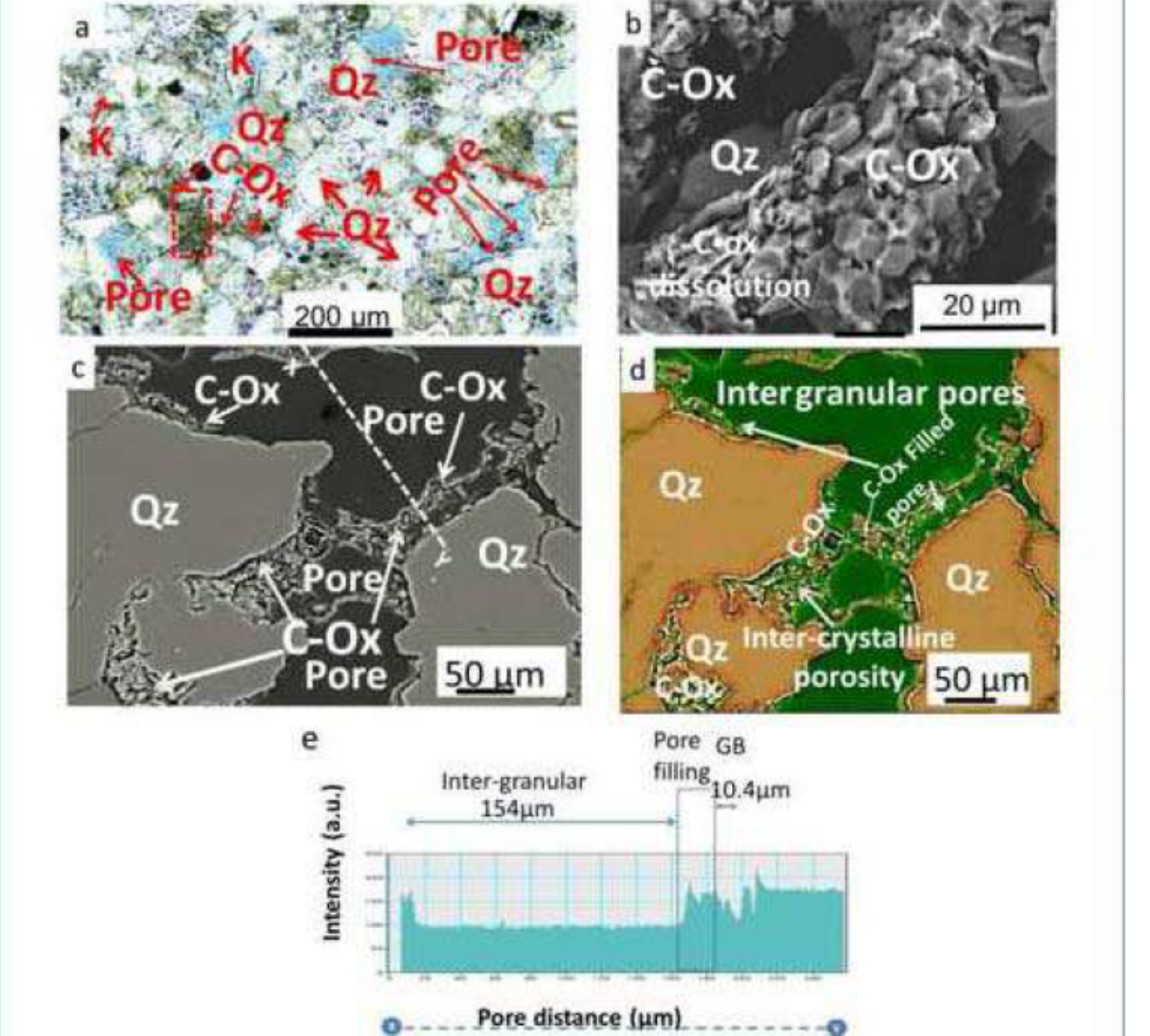
a
K
Qz
Pore
K
Qz
C-Ox
Pore
Qz
Pore
Qz
200 µm
b
C-Ox
Qz
C-Ox
C-Ox
dissolution
20 µm
c
C-Ox
C-Ox
Pore
Qz
Qz
Pore
C-Ox
Pore
50 µm
d
Intergranular pores
C-Ox Filled
pore
Qz
C-Ox
Qz
Qz
Inter-crystalline
porosity
50 µm
e
Pore
filling
GB
Inter-granular
154µm
10.4µm
Intensity (a.u.)
Pore distance (µm)

Figure 12

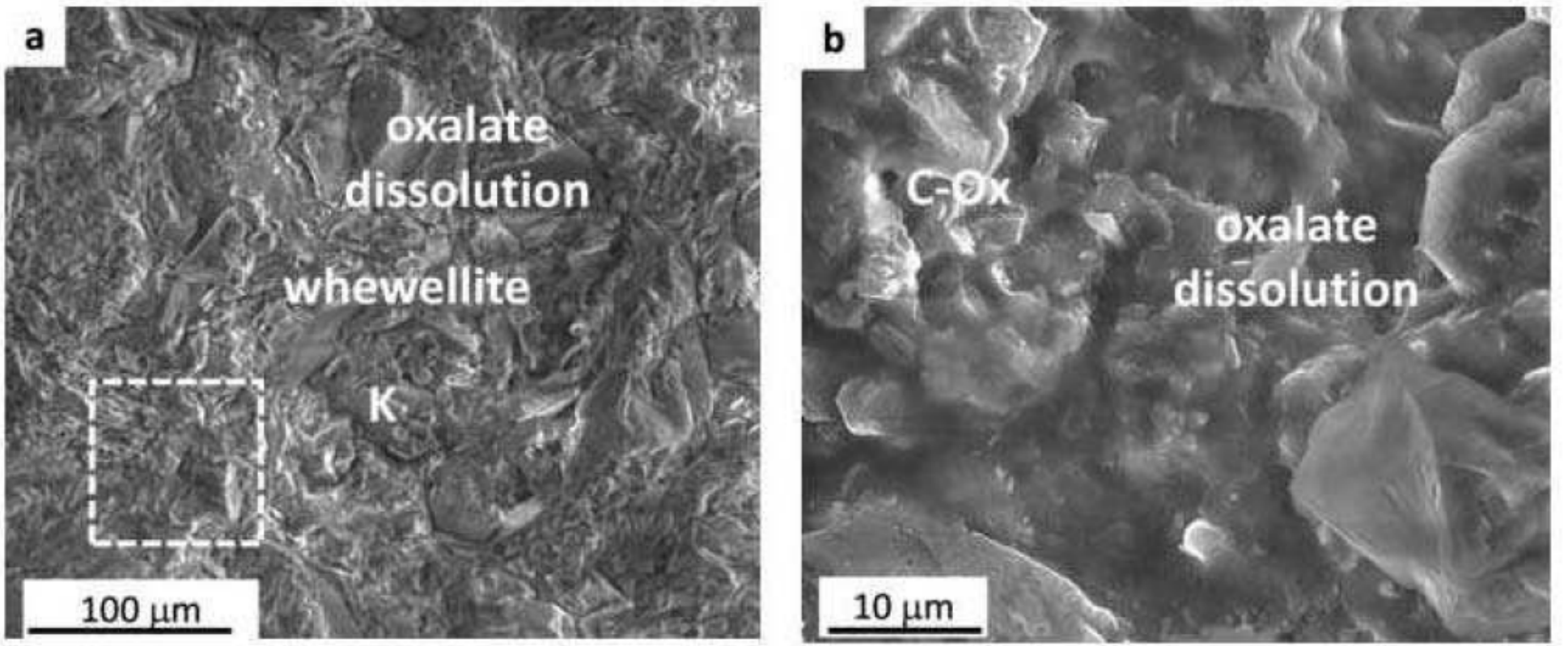
a
oxalate
dissolution
whewellite
K
100 µm
b
C-Ox
oxalate
dissolution
10 µm

Figure 13

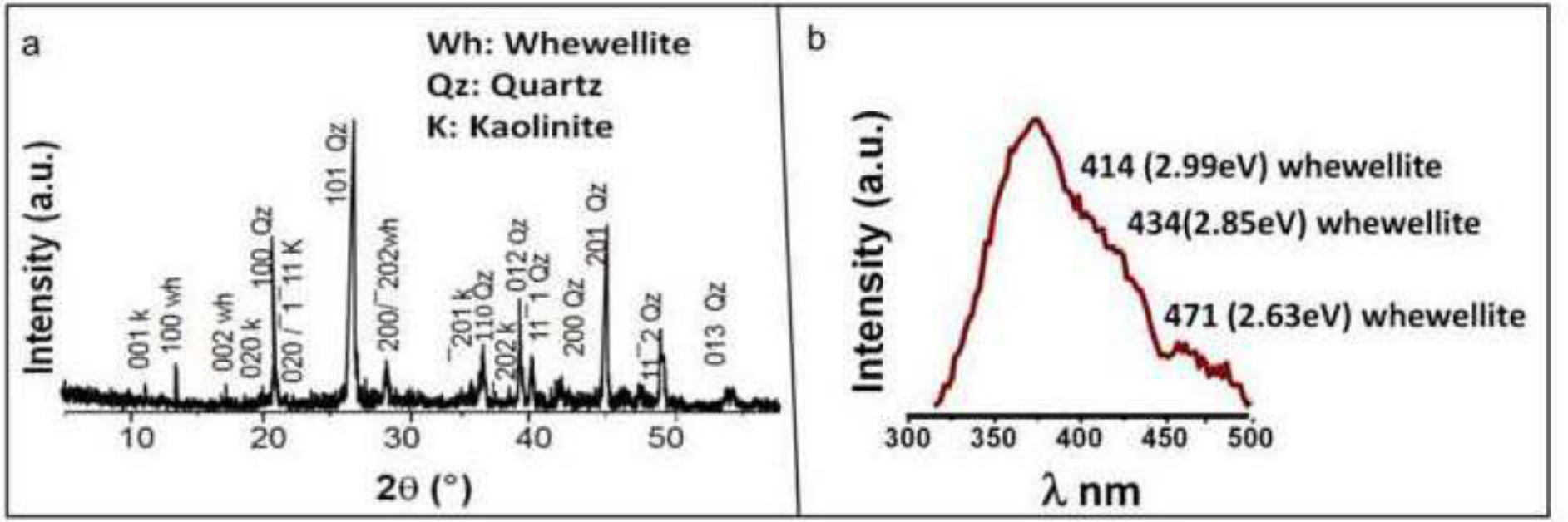
a
Wh: Whewellite
Qz: Quartz
K: Kaolinite
Intensity (a.u.)
001 k
100 wh
002 wh
020 k
100 Qz
020 / ¯1 ¯11 K
101 Qz
200/¯202wh
¯201 k
110 Qz
¯202 k
012 Qz
11¯1 Qz
200 Qz
201 Qz
11¯2 Qz
013 Qz
10
20
30
40
50
2θ (°)
b
Intensity (a.u.)
414 (2.99eV) whewellite
434(2.85eV) whewellite
471 (2.63eV) whewellite
300
350
400
450
500
λ nm

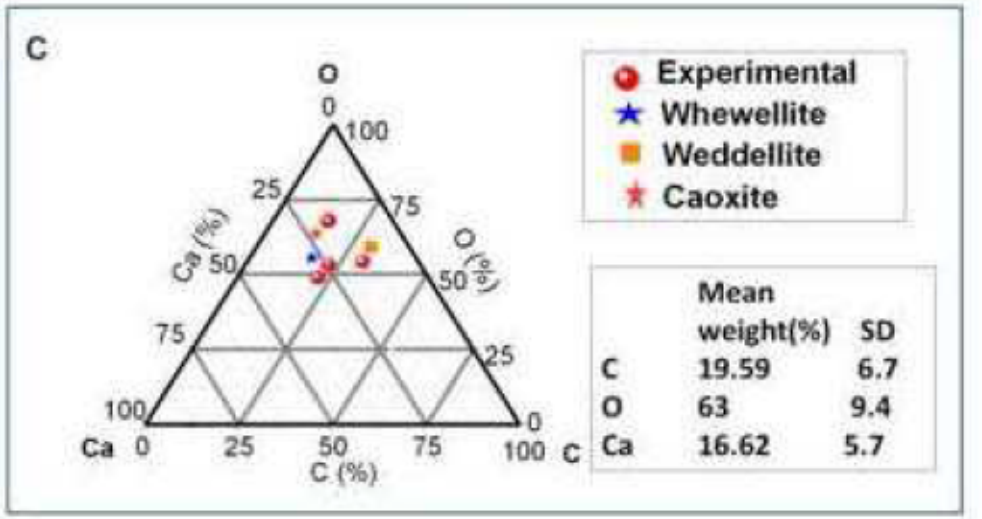
c
O
Ca (%)
O (%)
C (%)
Ca
C
Experimental
Whewellite
Weddellite
Caoxite
Mean weight(%) SD
C 19.59 6.7
O 63 9.4
Ca 16.62 5.7

Figure 14

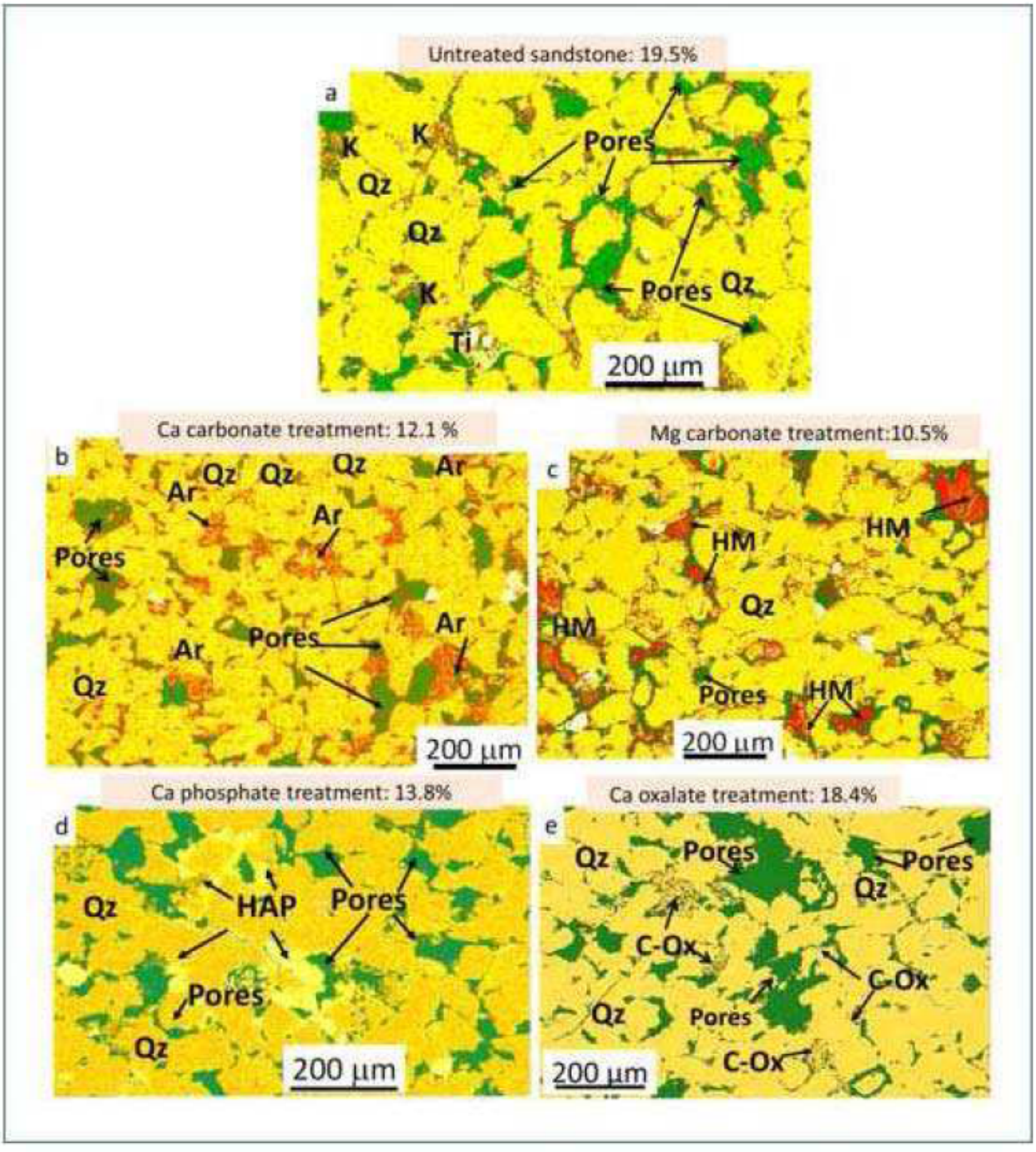
Untreated sandstone: 19.5%
a
K
K
Qz
Pores
Qz
K
Pores
Qz
Ti
200 µm
Ca carbonate treatment: 12.1 %
b
Qz
Qz
Qz
Ar
Ar
Ar
Pores
Pores
Ar
Ar
Qz
200 µm
Mg carbonate treatment:10.5%
c
HM
HM
Qz
HM
Pores
HM
200 µm
Ca phosphate treatment: 13.8%
d
Qz
HAP
Pores
Pores
Qz
200 µm
Ca oxalate treatment: 18.4%
e
Qz
Pores
Pores
Qz
C-Ox
C-Ox
Qz
Pores
C-Ox
200 µm

Figure 15

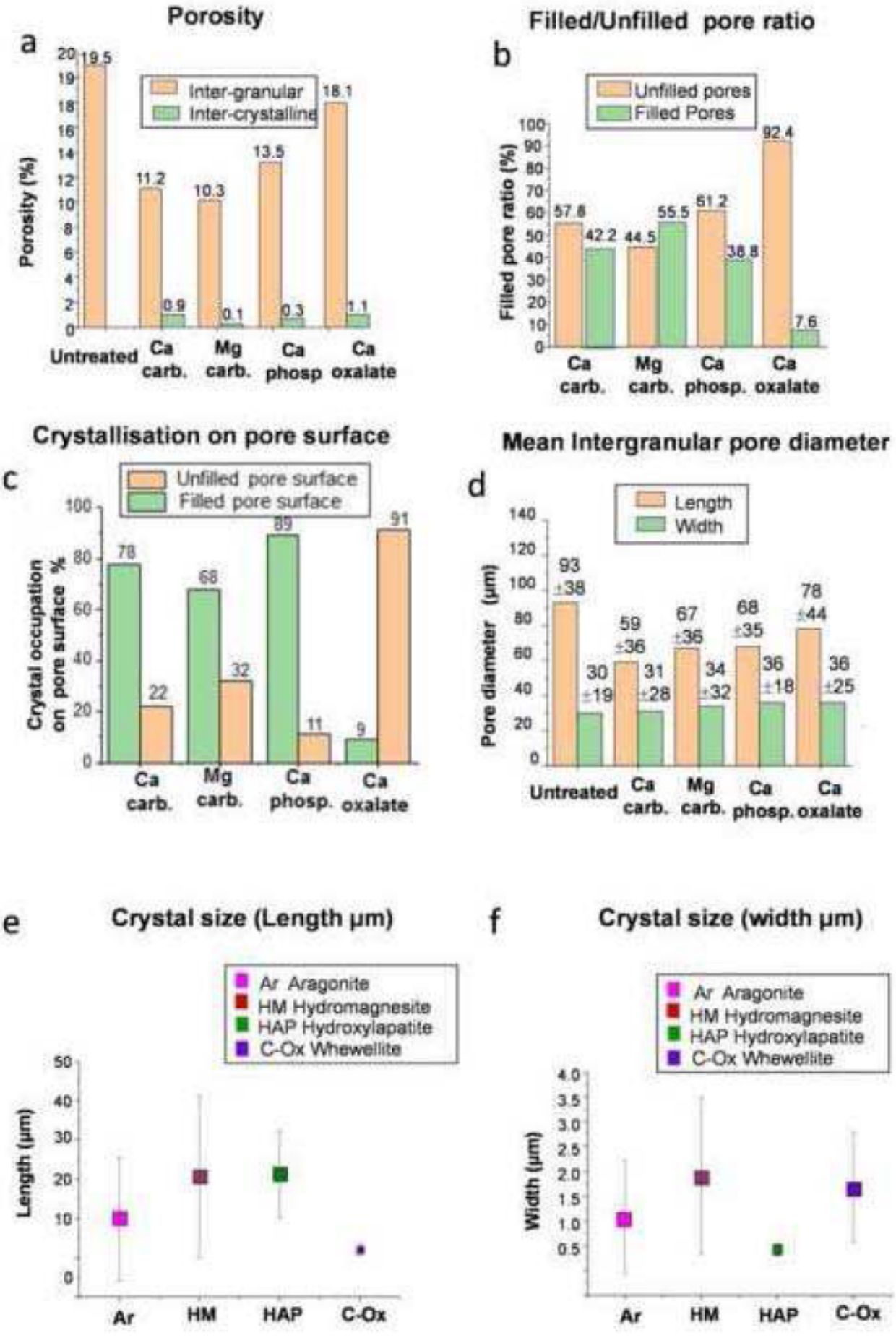
Porosity
a
Porosity (%)
Inter-granular
Inter-crystalline
19.5
11.2
0.9
10.3
0.1
13.5
0.3
18.1
1.1
Untreated
Ca carb.
Mg carb.
Ca phosp
Ca oxalate
Filled/Unfilled pore ratio
b
Filled pore ratio (%)
Unfilled pores
Filled Pores
57.8
42.2
44.5
55.5
61.2
38.8
92.4
7.6
Ca carb.
Mg carb.
Ca phosp.
Ca oxalate
Crystallisation on pore surface
c
Crystal occupation on pore surface %
Unfilled pore surface
Filled pore surface
78
22
68
32
89
11
9
91
Ca carb.
Mg carb.
Ca phosp.
Ca oxalate
Mean Intergranular pore diameter
d
Pore diameter (µm)
Length
Width
93 ±38
30 ±19
59 ±36
31 ±28
67 ±36
34 ±32
68 ±35
36 ±18
78 ±44
36 ±25
Untreated
Ca carb.
Mg carb.
Ca phosp.
Ca oxalate
e
Crystal size (Length µm)
Ar Aragonite
HM Hydromagnesite
HAP Hydroxylapatite
C-Ox Whewellite
Length (µm)
Ar
HM
HAP
C-Ox
f
Crystal size (width µm)
Ar Aragonite
HM Hydromagnesite
HAP Hydroxylapatite
C-Ox Whewellite
Width (µm)
Ar
HM
HAP
C-Ox